Coulomb correlations in 4d and 5d oxides from first principles—or how spin–orbit materials choose their effective orbital degeneracies

OPEN ACCESS
IOP Publishing
Journal of Physics: Condensed Matter
J. Phys.: Condens. Matter **29** (2017) 263001 (23pp)
https://doi.org/10.1088/1361-648X/aa648f

Topical Review

Coulomb correlations in 4d and 5d oxides from first principles—or how spin–orbit materials choose their effective orbital degeneracies

C Martins[1], M Aichhorn[2] and S Biermann[3]

[1] Laboratoire de Chimie et Physique Quantiques, UMR 5626, Université Paul Sabatier, 118 route de Narbonne, 31400 Toulouse, France
[2] Institute of Theoretical and Computational Physics, Technical University Graz, Petersgasse 16, Graz, Austria
[3] Centre de Physique Théorique, Ecole Polytechnique, CNRS UMR 7644, Université Paris-Saclay, 91128 Palaiseau, France

E-mail: silke.biermann@polytechnique.edu

Received 1 December 2016, revised 7 February 2017
Accepted for publication 6 March 2017
Published 26 May 2017

Abstract

The interplay of spin–orbit coupling and Coulomb correlations has become a hot topic in condensed matter theory and is especially important in 4d and 5d transition metal oxides, like iridates or rhodates. Here, we review recent advances in dynamical mean-field theory (DMFT)-based electronic structure calculations for treating such compounds, introducing all necessary implementation details. We also discuss the evaluation of Hubbard interactions in spin–orbit materials. As an example, we perform DMFT calculations on insulating strontium iridate (Sr_2IrO_4) and its 4d metallic counterpart, strontium rhodate (Sr_2RhO_4). While a Mott-insulating state is obtained for Sr_2IrO_4 in its paramagnetic phase, the spectral properties and Fermi surfaces obtained for Sr_2RhO_4 show excellent agreement with available experimental data. Finally, we discuss the electronic structure of these two compounds by introducing the notion of *effective spin–orbital degeneracy* as the key quantity that determines the correlation strength. We stress that effective spin–orbital degeneracy introduces an additional axis into the conventional picture of a phase diagram based on filling and on the ratio of interactions to bandwidth, analogous to the degeneracy-controlled Mott transition in d^1 perovskites.

Keywords: dynamical mean-field theory, electronic structure, iridates, rhodates, spin–orbit coupling

(Some figures may appear in colour only in the online journal)

1. Introduction

Electronic Coulomb correlations are at the heart of a variety of exotic properties in compounds with partially filled 3d or 4f shells. Prominent examples are found among the 3d transition metal oxides, where unconventional transport behaviors, ordering phenomena or unusual spectroscopic properties are observed [1]. It was argued early on that the comparably weak spatial extension of 3d orbitals leads to large electronic Coulomb interactions, competing with kinetic contributions. Depending on crystal fields, hybridisation, Hund's exchange, and band filling, this interplay can lead to renormalized metallic behavior such as in simple oxides like $SrVO_3$ [2, 3] or iron pnictide compounds [4–9] or induce Mott insulating behavior like in $YTiO_3$ [10] or V_2O_3 [11–14]. According to common belief held until recently, such effects would be less dramatic in 4d, and even less so in 5d compounds, due to the substantially more extended radial wave functions of those shells, as shown in figure 1. The discovery of Mott insulating behavior in Sr_2IrO_4 therefore triggered a little revolution in the field [15, 16]. In 5d oxides, spin–orbit coupling acts on an energy scale comparable to the other scales of the system (Coulomb interactions, bandwidths, ligand fields...), and the electronic state is the result of a complex interplay of Coulomb correlations, spin–orbit splitting and crystal field effects (for recent reviews, see [17, 18]). But, as pointed out earlier [19, 20], spin–orbit interactions can also influence the electronic properties substantially in 4d compounds. In Sr_2RhO_4, for example, the experimentally observed Fermi surface can only be reconciled with experiments when spin–orbit coupling and electronic Coulomb correlations are taken into account [19–22]. Here, we give a review of recent efforts to describe correlated spin–orbit physics from first principles, in a combined density functional and dynamical mean-field theory framework [21].

2. Spin–orbit materials—an incomplete literature review

The term *spin–orbit material* refers to systems where spin–orbit coupling (SOC) and its interplay with other elements of the electronic structure—crystal or ligand fields, Coulomb correlations, magnetism,...—is essential in determining the physical properties. In many such materials, the physics is largely determined by the geometrical aspects of the crystalline structure, and the electronic properties can be understood by analysing the one-particle band structure. In particular, strong enough spin–orbit coupling can cause band inversions, possibly leading to non-trivial topological effects. The quest for topological materials is nowadays a hot topic of condensed matter physics, and several excellent reviews exist in the literature [23–25].

The scope of the present review is, however, a different one. Here, we focus on materials, where the interplay of spin–orbit interactions and Coulomb correlations is crucial, and the band picture is at best useful as a starting point for further many-body calculations. Early examples are found among the layered tantalum chalcogenides: TaS_2 [26–28] is Mott

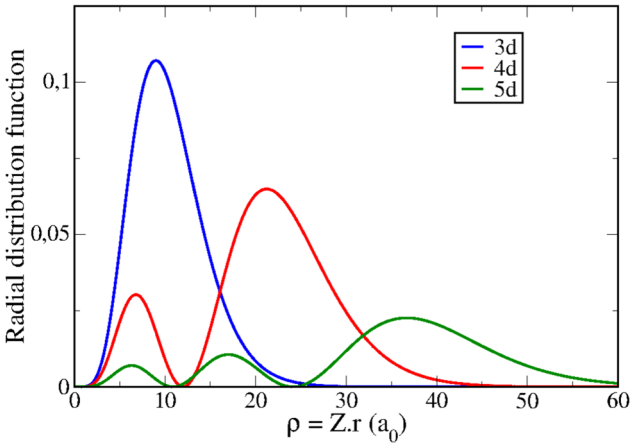

Figure 1. Radial distribution function $r^2R_{n\ell}(r)^2$ as a function of the distance from the nucleus r expressed in atomic units, for the $3d$, $4d$ and $5d$ orbitals. To ease the comparison between different atoms, we use the renormalized distance $\rho = Z \cdot r$ on the abscissa, where Z is the effective nuclear charge for a given multi-electron atom. As the principal quantum number n increases, Z remains almost constant for d valence electrons and their radial distribution is thus more and more extended.

insulating thanks to the presence of a lone narrow band resulting from the combined effect of SOC and a charge-density wave instability. The corresponding selenide, $TaSe_2$, [29] displays a surface Mott metal–insulator transition. Nevertheless, the true power of the interplay of spin–orbit interactions was fully appreciated only after the discovery of Sr_2IrO_4: the insulating behavior—despite moderate Coulomb interactions usually present in 5d compounds—was even more intriguing, as the electronic and crystal structures are otherwise seemingly simple. The interplay of Coulomb correlations and spin–orbit coupling was indeed shown to be essential in driving the system insulation, leading to a state dubbed 'spin–orbit Mott insulator' [15, 16]. A flurry of further spin–orbit materials have by now been characterized, or known compounds have been reinvestigated in the light of the new insights. Iridium-based materials, where several families of compounds have been studied systematically, still hold a privileged position. Table 1 summarizes the structural, transport and magnetic properties of a selection of iridates. It is interesting to note that the large majority among them display insulating phases. The Ir^{4+} ($5d^5$) state does not allow for a band insulating state without symmetry breaking, and magnetic order is an obvious candidate for helping to open the gap. Nevertheless, few compounds have been unambiguously characterized as Slater insulators.

Slightly more recently, attention focused on yet another class of 5d materials, namely osmium-based compounds. In this class fall, for example, ferroelectric $LiOsO_3$ [30], as well as the prototypical Slater insulator $NaOsO_3$ [31–36], where the loss of magnetic order with increasing temperature is accompanied by a closure of the insulating gap. It has been realized, however, that SOC can also have notable effects in 4d compounds, with prominent examples among ruthenium- and rhodium-based materials, where most interesting consequences for magnetic excitations have been discussed [37]. Table 2 gives an overview of the properties of a selection of

Table 1. Main structural, transport and magnetic properties of Ir-based spin–orbit materials. In the third column, Ins. refers to *insulator* and MIT to *metal–insulator transition*. The notations AFM, FM and AIAO refer to an *antiferromagnetic*, *ferromagnetic* and *all-in-all-out* magnetic ordering, respectively.

Iridium-based spin–orbit materials								
Compound	Crystal struct.		Transport property		Magnetic ordering			Reference
$CaIrO_3$	Post-perovskite	*Cmcm*	Ins.	gap: 0.34 eV	AFM		$T_N = 115$ K	[38–40]
$NaIrO_3$	Post-perovskite	*Cmcm*	Ins.	—		None		[41, 42]
$BaIrO_3$	Monoclinic	*C*2/*m*	Ins.	gap: 0.05 eV	FM		$T_C = 180$ K	[43–45]
$SrIrO_3$	Monoclinic	*C*2/*c*	Metal			None		[46–49]
α-Na_2IrO_3	Honeycomb monoclinic	*C*2/*c*	Ins.	gap: 0.35 eV	Zig-zag AFM		$T_N = 15$ K	[50–55]
α-Li_2IrO_3	Honeycomb monoclinic	*C*2/*c*	Ins.	—	Spiral AFM		$T_N = 15$ K	[56, 57]
β-Li_2IrO_3	Hyperhoneycomb	*Fddd*	Ins.	—	Unconventional AFM		$T_N = 38$ K	[58, 59]
γ-Li_2IrO_3	Stripyhoneycomb	*Cccm*	Ins.	—	Unconventional AFM		$T_N = 38$ K	[60]
Ba_2IrO_4	K_2NiF_4-type	*I*4/*mmm*	Ins.	gap: 0.14 eV	AFM		$T_N = 240$ K	[61–64]
Sr_2IrO_4	Distorted K_2NiF_4-type	$I4_1/acd$	Ins.	gap 0.25 eV	Canted AFM		$T_N = 240$ K	[15, 16, 21]
Ca_4IrO_6	Hexagonal	$R\bar{3}c$	Ins.	—	AFM		$T_N = 13.95$ K	[65–67]
$Y_2Ir_2O_7$	Pyrochlore	$Fd\bar{3}m$	Ins.	—	AIAO		$T = 155$ K	[68, 69]
$Pr_2Ir_2O_7$	Pyrochlore	$Fd\bar{3}m$	Metal			None		[70, 71]
$Nd_2Ir_2O_7$	Pyrochlore	$Fd\bar{3}m$	MIT	$T = 36$ K	AIAO		$T = 36$ K	[70, 72]
$Sm_2Ir_2O_7$	Pyrochlore	$Fd\bar{3}m$	MIT	$T = 117$ K	AIAO		$T = 117$ K	[70, 72]
$Eu_2Ir_2O_7$	Pyrochlore	$Fd\bar{3}m$	MIT	$T = 120$ K	AIAO		$T = 120$ K	[70, 73–75]
$Gd_2Ir_2O_7$	Pyrochlore	$Fd\bar{3}m$	Ins.	—	AIAO		$T = 127$ K	[70]
$Tb_2Ir_2O_7$	Pyrochlore	$Fd\bar{3}m$	Ins.	—	AIAO		$T = 130$ K	[70, 76]
$Dy_2Ir_2O_7$	Pyrochlore	$Fd\bar{3}m$	Ins.	—	AIAO		$T = 134$ K	[70]
$Ho_2Ir_2O_7$	Pyrochlore	$Fd\bar{3}m$	Ins.	—	AIAO		$T = 141$ K	[70]
$Er_2Ir_2O_7$	Pyrochlore	$Fd\bar{3}m$	Ins.	—	AIAO		$T = 140$ K	[76]
$Yb_2Ir_2O_7$	Pyrochlore	$Fd\bar{3}m$	Ins.	—	AIAO		$T = 130$ K	[77]
$Lu_2Ir_2O_7$	Pyrochlore	$Fd\bar{3}m$	Ins.	—	AIAO		$T = 120$ K	[78]
$Bi_2Ir_2O_7$	Pyrochlore	$Fd\bar{3}m$	Metal			None		[79, 80]
$Sr_3Ir_2O_7$	Monoclinic	*C*2/*c*	Ins.	gap: 0.1 eV	AFM		$T_N = 285$ K	[46, 81–85]
$Na_4Ir_3O_8$	Hyperkagome	$P4_132$	Ins.	—	AFM		$T_N = 6$ K	[86–88]
$Ca_5Ir_3O_{12}$	Hexagonal	$P-62m$	Ins.	—	AFM		$T_N = 7.8$ K	[66, 67, 89]
La_2ZnIrO_6	Double-perovskite	$P2_1/n$	Ins.	—	FM		$T_C = 7.5$ K	[90]
La_2MgIrO_6	Double-perovskite	$P2_1/n$	Ins.	gap: 0.16 eV	AFM		$T_N = 12$ K	[90, 91]
Pr_2MgIrO_6	Double-perovskite	$P2_1/n$	Ins.	gap: 0.2 eV	AFM		$T_N = 14$ K	[91, 92]
Nd_2MgIrO_6	Double-perovskite	$P2_1/n$	Ins.	—	AFM		$T_N = 12$ K	[92]
Sm_2MgIrO_6	Double-perovskite	$P2_1/n$	Ins.	—	AFM		$T_N = 15$ K	[92]
Eu_2MgIrO_6	Double-perovskite	$P2_1/n$	Ins.	—	AFM		$T_N = 10$ K	[92]
Gd_2MgIrO_6	Double-perovskite	$P2_1/n$	Ins.	—		None		[92]
Sr_2CeIrO_6	Double perovskite	$P2_1/n$	Ins.	gap: 0.3 eV	AFM		$T_N = 21$ K	[93–95]
Ba_2YIrO_6	Double perovskite	$Fm\bar{3}m$	Ins.	gap: 0.221 eV		None		[96]
$Ba_3IrTi_2O_9$	Hexagonal	$P6_3mc$	Ins.	—		None		[97, 98]
$Ba_3ScIr_2O_9$	Hexagonal	$P6_3/mmc$	Ins.	—		None		[99]
$Ba_3YIr_2O_9$	Hexagonal	$P6_3/mmc$	Ins.	—	FM		$T = 4$ K	[99]
$Ba_3ZnIr_2O_9$	Hexagonal	$P6_3/mmc$	Ins.	—		None		[100]

osmates, ruthenates and rhodates. In the following discussion, we will restrict ourselves to the prototypical correlated iridate Sr_2IrO_4 and its 4d analog, Sr_2RhO_4.

2.1. Correlated spin–orbit insulators: the example of Sr_2IrO_4

The 5d transition metal oxide (TMO) Sr_2IrO_4 has a tetragonal crystal structure, the symmetry of which is lowered from the K_2NiF_4-type, well-known in Sr_2RuO_4 or La_2CuO_4, by an 11° rotation of its IrO_6 octahedra around the **c**-axis [136]. Each Ir atom accommodates 5 electrons and the standard picture neglecting spin–orbit interactions would give a 't_{2g}^5' ground state. However, this compound exhibits insulating behavior up to the highest measured temperatures, with a strongly temperature-dependent gap. The optical gap at room temperature is about 0.26 eV [137]. Below $T_N = 240$ K, a canted-antiferromagnetic (AF) order sets in, with an

Table 2. Main structural, transport and magnetic properties of Ru, Rh and Os-based spin–orbit materials. In the third column, Ins. refers to *insulator* and MIT to *metal–insulator transition*. The notations AFM, FM and AIAO refer to an *antiferromagnetic*, *ferromagnetic* and *all-in-all-out* magnetic ordering, respectively.

Compound	Crystal struct.		Transport property		Magnetic ordering		Reference
		Ruthenium-based spin–orbit materials					
$BaRuO_3$	Cubic perovskite	$Pm\bar{3}m$	Metal		FM	$Tc = 60$ K	[101–103]
$CaRuO_3$	Perovskite	*Pnma*	Metal			None	[104–106]
$SrRuO_3$	Perovskite	*Pnma*	Metal		FM	$T_c = 160$ K	[104, 106, 107]
Sr_2RuO_4	K_2NiF_4-type	*I4/mmm*	Metal			None	[108, 109]
Ca_2RuO_4	Distorted K_2NiF_4-type	*Pbca* or $P2_1/c$	MIT	$T = 357$ K	AFM	$T = 110$ K	[108, 110–112]
$SrRu_2O_6$	Hexagonal	$P\bar{3}1m$	Ins.	—	AFM	$T_N = 565$ K	[113, 114]
$Sr_3Ru_2O_7$	Orthorhombic	*BBcb*	Metal			None	[106, 115]
$Sr_4Ru_3O_{10}$	Orthorhombic	*Pbam*	Metal		FM	$T_c = 105$ K	[106, 116, 117]
		Rhodium-based spin–orbit materials					
Li_2RhO_3	Honeycomb	$C2/m$	Ins.	gap: 0.08 eV		None	[118, 119]
Sr_2RhO_4	Distorted K_2NiF_4-type	$I4_1acd$	Metal			None	[21, 120, 121]
Sr_4RhO_6	Hexagonal	$R\bar{3}c$	Ins.	gap: 0.1 eV	AFM	$T_N = -$ K	[122]
$Sr_5Rh_4O_{12}$		$P3c1$	Ins.	—	AFM	$T_N = 23$ K	[66, 123]
		Osmium-based spin–orbit materials					
$BaOsO_3$	Six-layer hexagonal 6H	$Pm\bar{3}m$	Metal			None	[124, 125]
$CaOsO_3$	Perovskite	*Pnma*	Metal			None	[125]
$SrOsO_3$	Perovskite	*Pnma*	Metal			None	[125]
$NaOsO_3$	Perovskite	*Pnma*	MIT	$T = 410$ K	AFM	$T = 410$ K	[31–36]
$Cd_2Os_2O_7$	Pyrochlore	$Fd\bar{3}m$	MIT	$T = 226$ K	AIAO	$T = 226$ K	[126–129]
Ba_2NaOsO_6	Double-perovskite	$Fm\bar{3}m$	Ins.	—	FM	$T_c = 6.8$ K	[130–132]
Ba_2LiOsO_6	Double-perovskite	$Fm\bar{3}m$	Ins.	—	AFM	$T_N = 8$ K	[131]
Ba_2CaOsO_6	Double-perovskite	$Fm\bar{3}m$	Ins.	—	FM	$T_c = 50$ K	[133, 134]
Ba_2YOsO_6	Double-perovskite	$Fm\bar{3}m$	Ins.	—	AFM	$T_N = 69$ K	[134, 135]

effective local moment of 0.5 μ_B/Ir, and a saturation moment of 0.14 μ_B/Ir [138]. This phase has triggered much experimental and theoretical work [139–142], highlighting, in particular, the importance of the SOC.

Here, we focus on the paramagnetic phase, above 240 K, which is most interesting due to the persistence of the insulating nature despite the absence of magnetic order, as shown by transport measurements [15], by scanning tunneling microscopy and spectroscopy experiments [143], by angle-resolved spectroscopy [16, 144], time-resolved spectroscopy [145, 146] or optical conductivity [137].

Resonant inelastic x-ray spectroscopy (RIXS) experiments [15] proposed a picture early on in terms of $j_{\rm eff} = 1/2$ states and $j_{\rm eff} = 3/2$ states:

$$\left|j_{\rm eff} = \frac{1}{2}, m_{j_{\rm eff}} = +\frac{1}{2}\right\rangle = +\frac{1}{\sqrt{3}}(\left|d_{yz},\downarrow\right\rangle + \mathrm{i}\left|d_{xz},\downarrow\right\rangle) + \frac{1}{\sqrt{3}}\left|d_{xy},\uparrow\right\rangle,$$

$$\left|j_{\rm eff} = \frac{1}{2}, m_{j_{\rm eff}} = -\frac{1}{2}\right\rangle = +\frac{1}{\sqrt{3}}(\left|d_{yz},\uparrow\right\rangle - \mathrm{i}\left|d_{xz},\uparrow\right\rangle) - \frac{1}{\sqrt{3}}\left|d_{xy},\downarrow\right\rangle, \quad (1)$$

$$\left|j_{\rm eff} = \frac{3}{2}, m_{j_{\rm eff}} = +\frac{1}{2}\right\rangle = -\frac{1}{\sqrt{6}}(\left|d_{yz},\downarrow\right\rangle + \mathrm{i}\left|d_{xz},\downarrow\right\rangle) + \sqrt{\frac{2}{3}}\left|d_{xy},\uparrow\right\rangle,$$

$$\left|j_{\rm eff} = \frac{3}{2}, m_{j_{\rm eff}} = -\frac{1}{2}\right\rangle = +\frac{1}{\sqrt{6}}(\left|d_{yz},\uparrow\right\rangle - \mathrm{i}\left|d_{xz},\uparrow\right\rangle) + \sqrt{\frac{2}{3}}\left|d_{xy},\downarrow\right\rangle,$$

$$\left|j_{\rm eff} = \frac{3}{2}, m_{j_{\rm eff}} = +\frac{3}{2}\right\rangle = -\frac{1}{\sqrt{2}}(\left|d_{yz},\uparrow\right\rangle + \mathrm{i}\left|d_{xz},\uparrow\right\rangle),$$

$$\left|j_{\rm eff} = \frac{3}{2}, m_{j_{\rm eff}} = -\frac{3}{2}\right\rangle = +\frac{1}{\sqrt{2}}(\left|d_{yz},\downarrow\right\rangle - \mathrm{i}\left|d_{xz},\downarrow\right\rangle). \quad (2)$$

Since the quartet of states lies lower in energy than the doublet and the splitting between the $j_{\rm eff} = 3/2$ and $j_{\rm eff} = 1/2$ is large, neglecting any band dispersion would result in a configuration with one electron in the $j_{\rm eff} = 1/2$ state. The DFT band structure displays a dispersion of width comparable to this splitting, leaving the question *a priori* open again. However, the bandwidth is narrowed due to structural distortions [21], and electronic correlations can then become effective and eventually drive the compound insulation.

Since the discovery of this mechanism, other Ir-based compounds (see table 1) have been classified as spin–orbit Mott insulators (Na_2IrO_3, pyrochlores, etc...). Recent theoretical studies also predict some fluoride material [147] to be in this class. The one-orbital nature of insulating Sr_2IrO_4 has contributed to intense activities attempting to dope the compound,

with the hope of inducing a superconducting state as in the cuprates. Doping-induced metal–insulator transitions and the properties of the metallic phases have therefore become a hot topic, with studies of various compounds, e.g. Sr_2IrO_4 [144, 148], $(Sr_{1-x}La_x)_3Ir_2O_7$ [149], $Ca_{1-x}Sr_xIrO_3$ [150], $Ca_{1-x}Ru_xIrO_3$ [151], $Sr_2Ir_{1-x}Rh_xO_4$ [152, 153], $Sr_2Ir_{1-x}Ru_xO_4$ [154], $Sr_xLa_{11-x}Ir_4O_{24}$ [155].

2.2. Correlated spin–orbit metals: the example of Sr_2RhO_4

It is natural that also in *metallic* 4d or 5d transition metal compounds, SOC can have notable consequences. An example of a 'spin–orbit correlated metal' is the end member $SrIrO_3$ of the Ir-based Ruddlesden–Popper $Sr_{n+1}Ir_nO_{3n+1}$ series [46] but also many Ru-,Rh- or Os-based transition metal oxides (TMOs) belong to this class (see tables 1 and 2). In these compounds, correlations are important enough to renormalize the Fermi surface-, albeit in a strongly spin–orbit coupling-dependent way. The respective roles of both effects have been worked out in some detail for several compounds, among which are $SrIrO_3$ [46–48], Sr_2RuO_4/Ca_2RuO_4 [108, 109, 156] and Sr_2RhO_4 [19–21].

We will focus our attention in the following on Sr_2RhO_4, motivated by its structural proximity and isoelectronic nature to Sr_2IrO_4. Indeed, this TMO is the 4d counterpart of Sr_2IrO_4, both concerning structure and filling. To understand its Fermi surface requires the inclusion of both SOC and correlations [21]. It is composed of three pockets (see figure 8): a circular hole-like α-pocket around Γ, a lens-shaped electron pocket β_M and a square-shaped electron pocket β_X with a mass enhancement of 3.0, 2.6 and 2.2, respectively [120].

In this review, we will put Sr_2IrO_4 and Sr_2RhO_4 in parallel, shedding light on the spectral properties of these compounds and elaborating on the notion of a reduced effective (spin–orbital) degeneracy that is crucial for their properties.

2.3. Spin–orbit coupling and cubic symmetry: the j_{eff} picture

Necessary conditions for realizing a j_{eff} picture are (1) a strong spin–orbit coupling constant and (2) an important cubic crystal field. These conditions are often met in crystalline structures where IrO_6 octahedra are present (see table 1). Similar compounds based on Ru, Rh and Os also show such j_{eff} states (see table 2). However, not all Ir-based structures belong to this case: we note that neither epitaxial thin films of IrO_2 [157] nor the correlated metal IrO_2 in its rutile structure [158, 159] exhibit such a $j_{eff} = 1/2$ state. We will now turn to a more precise description of that picture.

The spin–orbit interaction is one of the relativistic corrections to the Schrödinger–Pauli equation arising when taking the non-relativistic limit of Dirac's equation. It introduces a coupling between the spin $\mathbf{S}$ and the motion—or, more precisely, the orbital momentum $\mathbf{L}$ in the atomic case—of the electron. In a solid described within an independent-particle picture, spin–orbit coupling has the following general form:

Table 3. Value of the spin–orbit constant ζ_{SO} in the d-valence shells of some transition metals. Data from Landolt–Börnstein database and [160] (3d), from [19, 161] (4d) and from [162] (5d).

Atom	Z	$\zeta_{SO}(3d)$ (eV)	Atom	Z	$\zeta_{SO}(4d)$ (eV)	Atom	Z	$\zeta_{SO}(5d)$ (eV)
Fe	26	0.050	Ru	44	0.161	Os	76	0.31
Co	27	0.061	Rh	45	0.191	Ir	77	0.40
Cu	29	0.103	Ag	47	0.227	Au	79	0.42

$$H_{SO} = \frac{\hbar}{4m_0^2c^2}\boldsymbol{\sigma}\cdot[\boldsymbol{\nabla}V(\mathbf{r})\times\mathbf{p}], \tag{3}$$

where m_0 is the electron mass, $V(\mathbf{r})$ is the effective Kohn–Sham potential and $\sigma_{i=x,y,z}$ denote the Pauli-spin matrices. Assuming that the potential close to the nucleus has spherical symmetry, the mean value of the spin–orbit interaction on the atomic state (n,ℓ) takes the more common form:

$$H_{SO} = \zeta_{SO}(n\ell)\,\mathbf{l}\cdot\mathbf{s}, \qquad \zeta_{SO}(n\ell) = \frac{\hbar^2}{2m_0^2c^2}\left\langle\frac{1}{r}\frac{dV}{dr}\right\rangle_{(n,\ell)}, \tag{4}$$

where $\mathbf{S} = \frac{1}{2}\boldsymbol{\sigma}$, $\mathbf{L} = \mathbf{r}\times\mathbf{p} = \hbar\,\mathbf{l}$ and $\langle\ldots\rangle_{(n,\ell)}$ denotes the mean value of the radial quantity in the state (n,ℓ). Table 3 gives some values of the spin–orbit constant ζ_{SO} for $3d$, $4d$ and $5d$ atoms. The SOC increases with the atomic number, explaining why spin–orbit materials are mostly found in $5d$ and $4d$ TMOs.

Due to the effect of SOC, a multiplet splitting arises in the d-orbitals. Figure 2 shows the multiplet splitting of d-orbitals due to the spin–orbit coupling as a function of the strength of a cubic crystal field $\Delta = 10Dq$.

In spherical symmetry the fine structure is composed of a six-fold $J = 5/2$ multiplet (in red) and a $J = 3/2$ quartet of lower energy (in blue), following 'Landé's interval rule'. The presence of a cubic crystal field splits further the six-fold multiplet. Indeed, the spin–orbit interaction in the cubic basis (e_g and t_{2g} in green and light green, respectively, in figure 2) can be reduced to two five-dimensional submatrices:

$$\left(\begin{array}{ccccc} 0 & -\mathrm{i} & \mathrm{i} & \sqrt{3} & -1 \\ \mathrm{i} & 0 & -1 & -\mathrm{i}\sqrt{3} & -\mathrm{i} \\ -\mathrm{i} & -1 & 0 & 0 & -2\mathrm{i} \\ \hline \sqrt{3} & \mathrm{i}\sqrt{3} & 0 & 0 & 0 \\ -1 & \mathrm{i} & 2\mathrm{i} & 0 & 0 \end{array}\right)\cdot\frac{\zeta_{SO}}{2},$$

$$\left(\begin{array}{ccccc} 0 & \mathrm{i} & \mathrm{i} & -\sqrt{3} & 1 \\ -\mathrm{i} & 0 & 1 & -\mathrm{i}\sqrt{3} & -\mathrm{i} \\ -\mathrm{i} & 1 & 0 & 0 & 2\mathrm{i} \\ \hline -\sqrt{3} & \mathrm{i}\sqrt{3} & 0 & 0 & 0 \\ 1 & \mathrm{i} & -2\mathrm{i} & 0 & 0 \end{array}\right)\cdot\frac{\zeta_{SO}}{2}, \tag{5}$$

in the bases $\{d_{xz}\uparrow, d_{yz}\uparrow, d_{xy}\downarrow, d_{3z^2-r^2}\downarrow, d_{x^2-y^2}\downarrow\}$ and $\{d_{xz}\downarrow, d_{yz}\downarrow, d_{xy}\uparrow, d_{3z^2-r^2}\uparrow, d_{x^2-y^2}\uparrow\}$, respectively. After diagonalization, the total angular momentum J remains a good

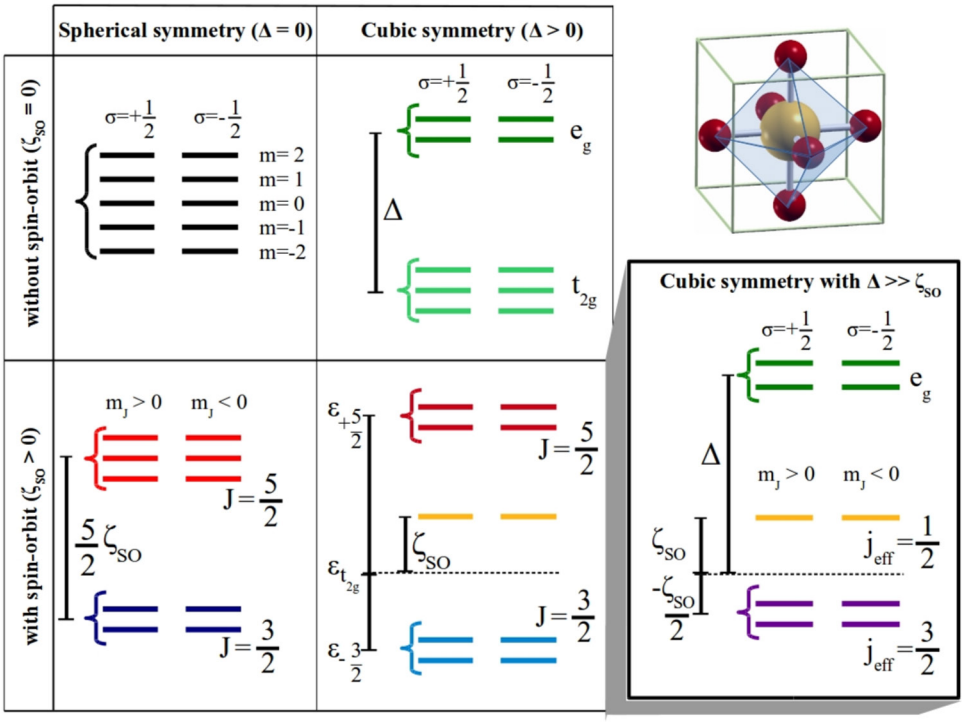

Figure 2. Orbital diagrams for the *d*-shell of an atom as a function of the cubic crystal field Δ and spin–orbit coupling ζ_{SO}, in a paramagnetic case. Starting from the *d*-shell in spherical symmetry, the cubic crystal field splits them into e_g and t_{2g}, while the SOC creates a six-fold $J = 5/2$ multiplet and a $J = 3/2$ quartet of lower energy. When both parameters are at stake, one gets a new multiplet structure where J remains a good quantum number but J_z does not. The initial $J = 5/2$ multiplet splits into a quartet and a doublet of lower energy, while the quartet $J = 3/2$ undergoes some redefinition inside its submanifold. The energetic splitting and the nature of the spin-orbitals depend on the ratio between Δ/ζ_{SO}. An exception is the doublet which is already of the form $j_{\text{eff}} = 1/2$. In the limit where $\Delta \gg \zeta_{SO}$, as is the case in the compounds of our interest, one gets the celebrated splitting into e_g, $j_{\text{eff}} = 1/2$ and $j_{\text{eff}} = 3/2$.

quantum number, contrary to j_z/m_j and one gets the following fine structure:

- a first quartet of $J = 5/2$ states (in red) with an energy

$$\varepsilon_{\frac{5}{2}+} = \frac{1}{4}(2\Delta - \zeta_{SO}) + \frac{1}{4}\sqrt{(2\Delta + \zeta_{SO})^2 + 24\zeta_{SO}^2},$$

- a doublet of $J = 5/2$ states (in yellow) of energy

$$\varepsilon_{\frac{5}{2}-} = +2\frac{\zeta_{SO}}{2},$$

- a quartet of $J = 3/2$ states (in light blue) with an energy

$$\varepsilon_{\frac{3}{2}} = \frac{1}{4}(2\Delta - \zeta_{SO}) - \frac{1}{4}\sqrt{(2\Delta + \zeta_{SO})^2 + 24\zeta_{SO}^2}.$$

In the limit of strong crystal field ($\Delta \gg \zeta_{SO}$), the $J = 5/2$ doublet (in yellow) remains invariant while the higher-energy quartet will tend to the usual e_g states and the lower-energy $J = 3/2$ quartet will be composed of t_{2g} states only, with an energy of $-\zeta_{SO}/2$.

Since the SOC matrix restricted to the t_{2g} subspace is exactly the opposite of the SOC matrix of the *p*-states of a free atom, one usually labels these latter states by a j_{eff} quantum number in analogy with the $p_{\frac{1}{2}}$ and $p_{\frac{3}{2}}$ multiplets, leading to the expressions given in equations (1) and (2). We point out that the $j_{\text{eff}} = 1/2$ doublet arises from the interplay of both cubic symmetry and SOC, whatever the strength of the crystal field. The corresponding eigenstates can indeed be written:

$$\begin{aligned}
\left|\frac{1}{2}, +\frac{1}{2}\right\rangle &= +\frac{1}{\sqrt{3}}(|d_{yz}, \downarrow\rangle + \mathrm{i}|d_{xz}, \downarrow\rangle) + \frac{1}{\sqrt{3}}|d_{xy}, \uparrow\rangle \\
&= \frac{i}{\sqrt{6}}\left(\sqrt{5}\left|\frac{5}{2}, -\frac{3}{2}\right\rangle - \left|\frac{5}{2}, \frac{5}{2}\right\rangle\right), \\
\left|\frac{1}{2}, -\frac{1}{2}\right\rangle &= +\frac{1}{\sqrt{3}}(|d_{yz}, \uparrow\rangle - \mathrm{i}|d_{xz}, \uparrow\rangle) - \frac{1}{\sqrt{3}}|d_{xy}, \downarrow\rangle \\
&= \frac{i}{\sqrt{6}}\left(\sqrt{5}\left|\frac{5}{2}, \frac{3}{2}\right\rangle - \left|\frac{5}{2}, -\frac{5}{2}\right\rangle\right)
\end{aligned} \tag{6}$$

(where the right hand side is written using the J,m_J quantum numbers). This may explain the robustness of this doublet in spin–orbit compounds [163]. However, the splitting between the $j_{\text{eff}} = 1/2$ and $j_{\text{eff}} = 3/2$ multiplets follows the inverse Landé interval rule (with the $j_{\text{eff}} = 1/2$ above the $j_{\text{eff}} = 3/2$ states) only in the strong crystal field limit.

3. Interplay of spin–orbit interaction and Coulomb correlations from first principles

3.1. DFT+ DMFT calculations with spin–orbit coupling

Combined density functional theory (DFT) and dynamical mean-field theory (DMFT), as pioneered in [164, 165] (for a review, see [166, 167]), has made correlated electron systems accessible to first principles calculations. Over the years, various classes of systems ranging from transition metals

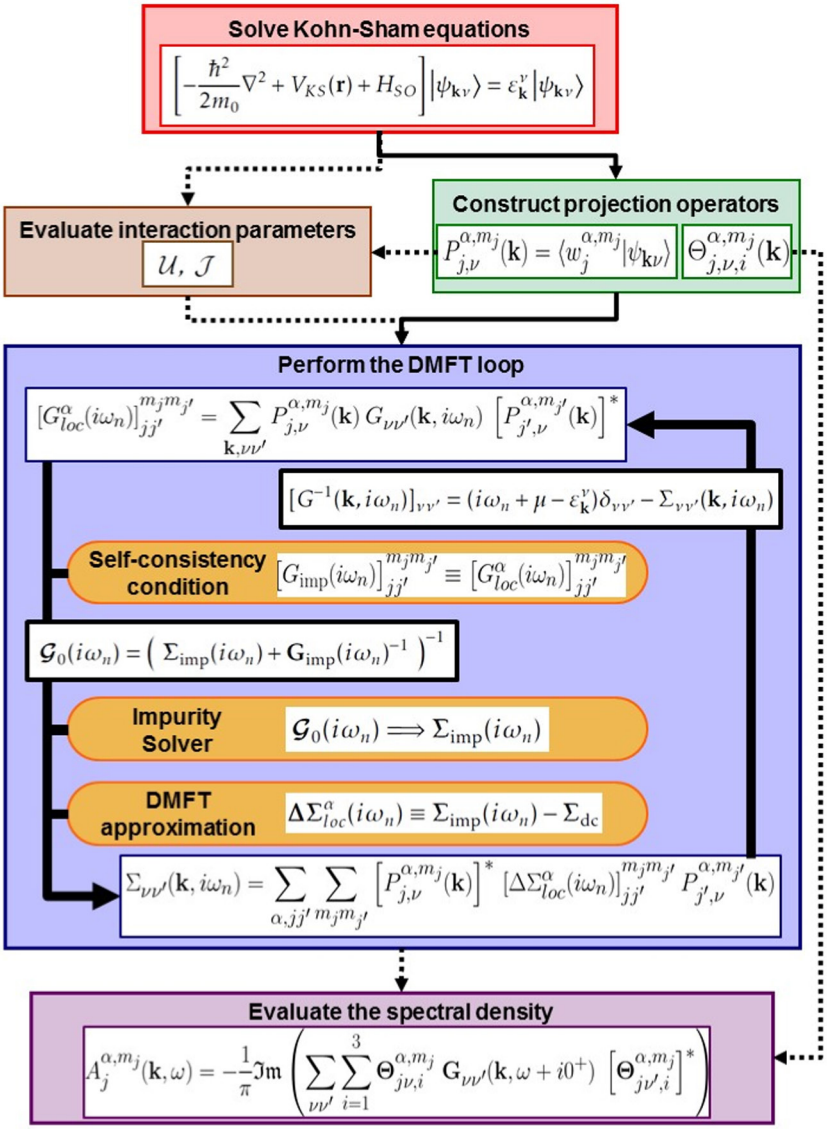

Figure 3. Projector-based implementation of DFT+DMFT for calculations including spin–orbit coupling in the Kohn–Sham equations. Once the Kohn–Sham eigenstates $|\psi_{\mathbf{k}\nu}\rangle$ are known, their projections $P^{\alpha,m_j}_{j,\nu}(\mathbf{k})$ to the correlated Wannier-like orbitals $|w^{\alpha,m_j}_{j}\rangle$ are calculated. One can then build an effective local many-body atomic problem, subject to a self-consistency condition, which is solved using an impurity solver: this defines the DMFT loop (see section 3.1). The interaction parameters can also be evaluated consistently using the projectors $P^{\alpha,m_j}_{j,\nu}(\mathbf{k})$ (see [204] and section 3.3). After convergence of the DMFT cycle, the chemical potential is updated and the spectral function can be evaluated using partial projectors $\Theta^{\alpha,m_j}_{j\nu,i}(\mathbf{k})$ (see appendix).

[168–171], their oxides [11, 172–177], sulphides [178, 179], pnictides [4, 9, 180, 181], rare earths [182–184] and their compounds [185–187], including heavy fermions [188, 189], actinides [190, 191] and their compounds [192, 193] to organics [194], correlated semiconductors [195, 196], and correlated surfaces and interfaces [197–199] have been studied with great success. Besides intensive methodological developments (see e.g. [2, 3, 167, 200–203]), recent research activities continue to extend to new classes of materials. In this context, 4d and 5d oxides have also come into focus [21, 22, 62]. In this section, we review the technical aspects related to combined DFT+DMFT calculations in the presence of spin–orbit interactions. Since the applications we later focus on are 4d and 5d oxides in their *paramagnetic* phases, we restrict the discussion to this case.

In DMFT, a local approximation is made to the many-body self-energy which can then be calculated from an effective atom problem, subject to a self-consistency condition (see figure 3).

The notion of locality is understood in the sense of many-body theory as a site-diagonal form, with respect to atomic sites after representing the Hamiltonian in an atom-centered Wannier-type basis $|w^{\alpha,\sigma}_{\ell m}\rangle$, where the index α labels the atom in the unit-cell, (ℓ, m) the angular momentum quantum numbers of the atomic orbital and σ the spin degree of freedom. Different choices are possible for the construction of the atom-centered orbitals, and the work reviewed here is based on the construction of projected atomic orbitals subject to a subsequent orthonormalization procedure [180].

The DMFT self-consistency cycle links the local effective atom problem to the electronic structure of the solid, via the transformation matrix from the Kohn–Sham states $|\psi^{\sigma}_{\mathbf{k}\nu}\rangle$, labelled by their momentum $\mathbf{k}$ their band index ν and their spin σ, to the resulting Wannier-like local orbitals $|w^{\alpha,\sigma}_{\ell m}\rangle$. These key quantities are called *projectors* and denoted $P^{\alpha,\sigma}_{\ell m,\nu}(\mathbf{k})$.

The main advantage of projector-based implementations of DFT+DMFT (see e.g. [180, 205, 206]) is that not only the DFT-based part of the calculations but also the determination of the local Green's function, used within the DMFT self-consistency condition, can be performed in any convenient basis set, and notably in the one used in the respective DFT code. Since the transformation of the DFT Hamiltonian matrix in that basis into the Kohn–Sham eigenset $|\psi^{\sigma}_{\mathbf{k}\nu}\rangle$ is known, it is sufficient to further determine the projections of the Kohn–Sham eigenstates onto the local orbitals $|w^{\alpha,\sigma}_{\ell m}\rangle$ used in the DMFT impurity problem. This is precisely the role of the projectors.

In [21], this construction was generalized to the case when spin is not a good quantum number anymore, and implemented within the framework of the DFT+DMFT implementation of [180]. Nowadays, it is available within the TRIQS/DFTTools package [207] that links the Wien2k code [208] to DMFT. We give here the main lines of this generalization of the projector-based DFT+DMFT formalism.

When taking into account SOC, the Kohn–Sham eigenstates $|\psi_{\mathbf{k}\nu}\rangle$ are built out of *both* spin-up and spin-down states—in a similar fashion to the previously introduced $j_{\text{eff}} = 1/2$ and $j_{\text{eff}} = 3/2$ atomic states. Nevertheless, we can still write them in the following Bloch form:

$$\begin{aligned}\psi_{\mathbf{k}\nu}(\mathbf{r}) &= [u^{\uparrow}_{\mathbf{k}\nu}(\mathbf{r}) + u^{\downarrow}_{\mathbf{k}\nu}(\mathbf{r})]\, \mathrm{e}^{\mathrm{i}\mathbf{k}\cdot\mathbf{r}} \\ &= \phi^{\uparrow}_{\mathbf{k}\nu}(\mathbf{r}) + \phi^{\downarrow}_{\mathbf{k}\nu}(\mathbf{r}),\end{aligned} \tag{7}$$

where the index ν now runs over *both* spin and band indices. The state $|\phi^{\sigma}_{\mathbf{k}\nu}\rangle$ denotes the projection of the Kohn–Sham state onto its spin-σ contribution and is *not* an eigenstate of the Hamiltonian.

Using this decomposition, we can define the new projectors:

$$P^{\alpha,\sigma}_{\ell m,\nu}(\mathbf{k}) = \langle w^{\alpha,\sigma}_{\ell m}|\psi_{\mathbf{k}\nu}\rangle = \langle w^{\alpha,\sigma}_{\ell m}|\phi^{\sigma}_{\mathbf{k}\nu}\rangle. \tag{8}$$

We define them in the standard complex basis, but allow for a basis transformation to quantum numbers j, m_j (like $j_{\text{eff}} = 1/2$ and $j_{\text{eff}} = 3/2$) afterwards by means of a unitary matrix transformation in the correlated ℓ-space:

$$P^{\alpha,m_j}_{j,\nu}(\mathbf{k}) = \sum_{m,\sigma} \mathcal{S}^{m_j,\sigma}_{j,\ell m}\langle w^{\alpha,\sigma}_{\ell m}|\psi_{\mathbf{k}\nu}\rangle = \sum_{m,\sigma} \mathcal{S}^{m_j,\sigma}_{j,\ell m} P^{\alpha,\sigma}_{\ell m,\nu}(\mathbf{k}). \tag{9}$$

The main difference with the usual implementation where spin is a good quantum number is that there are now two projectors associated with each band index ν: $P^{\alpha,\sigma}_{\ell m,\nu}(\mathbf{k})$ with $\sigma = \uparrow, \downarrow$.

Using the decomposition (7) in the formulation of the self-consistency condition relating the lattice Green's function of the solid to the impurity model, the (inverse) Green's function of the solid is given by:

$$[G^{-1}(\mathbf{k}, \mathrm{i}\omega_n)]_{\nu\nu'} = (\mathrm{i}\omega_n + \mu - \varepsilon^{\nu}_{\mathbf{k}})\delta_{\nu\nu'} - \Sigma_{\nu\nu'}(\mathbf{k}, \mathrm{i}\omega_n), \tag{10}$$

where $\varepsilon^{\nu}_{\mathbf{k}}$ are the (ν-dependent only) Kohn–Sham eigenvalues and $\Sigma_{\nu\nu'}(\mathbf{k}, \mathrm{i}\omega_n)$ is the approximation to the self-energy obtained by the solution of the DMFT impurity problem. It is obtained by 'mapping' the impurity self-energy to the local self-energy of the lattice and 'upfolding' it as:

$$\Sigma_{\nu\nu'}(\mathbf{k}, \mathrm{i}\omega_n) = \sum_{\alpha, jj'} \sum_{m_j m_{j'}} [P^{\alpha,m_j}_{j,\nu}(\mathbf{k})]^{*}\ [\Delta\Sigma^{\alpha}_{\text{loc}}(\mathrm{i}\omega_n)]^{m_j m_{j'}}_{jj'}\ P^{\alpha,m_{j'}}_{j',\nu'}(\mathbf{k}), \tag{11}$$

with

$$[\Delta\Sigma^{\alpha}_{\text{loc}}(\mathrm{i}\omega_n)]^{m_j m_{j'}}_{jj'} = [\Sigma_{\text{imp}}(\mathrm{i}\omega_n)]^{m_j m_{j'}}_{jj'} - [\Sigma_{\text{dc}}]^{m_j m_{j'}}_{jj'}. \tag{12}$$

Here, $\Sigma_{\text{imp}}(\mathrm{i}\omega_n)$ is the impurity self-energy, expressed in the local orbitals, and Σ_{dc} is the double-counting correction. Consequently, the equations of the DMFT loop (see figure 3) are formally the same as in the case without SOC, but the computations now involve matrices which are double in size.

The local Green's function is obtained by projecting the lattice Green's function to the set of correlated orbitals and summing over the full Brillouin zone,

$$[G^{\alpha}_{\text{loc}}(\mathrm{i}\omega_n)]^{m_j m_{j'}}_{jj'} = \sum_{\mathbf{k},\nu\nu'} P^{\alpha,m_j}_{j,\nu}(\mathbf{k})\, G_{\nu\nu'}(\mathbf{k}, \mathrm{i}\omega_n)\, [P^{\alpha,m_{j'}}_{j',\nu'}(\mathbf{k})]^{*}. \tag{13}$$

In practice, the summation over momenta is done in the irreducible Brillouin zone only, supplemented by a standard symmetrization procedure, using Shubnikov magnetic point groups [209, 210].

The DMFT equations are solved iteratively: starting from an initial local Green's function $G^{\alpha}_{\text{loc}}(\mathrm{i}\omega_n)$ (obtained from the 'pure' Kohn–Sham lattice Green's function using equation (13)), the Green's function $\mathcal{G}_0(\mathrm{i}\omega_n)$ of the effective environment in the impurity model is constructed. The impurity model is solved, allowing the evaluation of the local self-energy of the solid (see equation (11)) and a new lattice Green's function $G(\mathbf{k}, \mathrm{i}\omega_n)$. The latter can then be projected again onto the correlated subset and the cycle is repeated until convergence is reached.

3.2. Computation of the Wannier projectors within the augmented plane wave framework

The present implementation is within a full-potential linearized augmented plane wave (FLAPW) framework, as realized in the Wien2k package [208]. With respect to the existing DFT+DMFT implementation [180] in this context, the main changes concern the projection technique for building the correlated orbitals: as discussed above, one has to take care of the fact that spin is no longer a good quantum number, leading to the more general construction of localized 'spin-orbitals'. The necessary modifications in the construction of the projectors are reviewed in the following.

As in the case without SOC, we still use the Kohn–Sham states within a chosen energy window $\mathcal{W}$ to form the Wannier-like functions that are treated as correlated orbitals, and the construction of the Wannier projectors is done in two steps. First, auxiliary Wannier projectors $\widetilde{P}^{\alpha,\sigma}_{\ell m,\nu}(\mathbf{k})$ are calculated—separately for each $|\phi^{\sigma}_{\nu\mathbf{k}}\rangle$ term—from the following expression:

$$\widetilde{P}^{\alpha,\sigma}_{\ell m,\nu}(\mathbf{k}) = \langle u^{\alpha,\sigma}_{\ell}(E_1\ell) Y^{\ell}_{m} | \psi_{\mathbf{k}\nu} \rangle = A^{\nu\alpha}_{\ell m}(\mathbf{k},\sigma) + \sum_{n_{\mathrm{LO}}=1}^{N_{\mathrm{LO}}} c^{\nu,\sigma}_{\mathrm{LO}} C^{\alpha,\mathrm{LO}}_{\ell m} \mathcal{O}^{\alpha,\sigma}_{\ell m,\ell' m'}. \quad (14)$$

A description of the augmented plane wave (APW) basis can be found in [180]. We use the same notations e.g. for the coefficients $A^{\nu\alpha}_{\ell m}(\mathbf{k},\sigma)$ and the overlap matrix $\mathcal{O}^{\alpha,\sigma}_{\ell m,\ell' m'}$ as introduced there.

One performs an orthonormalization step in order to get the Wannier projectors $P^{\alpha,\sigma}_{\ell m,\nu}(\mathbf{k})$. The overlap matrix $[O(\mathbf{k})]^{\alpha,\alpha'}_{(m\sigma),(m'\sigma')}$ between the correlated ℓ orbitals is defined by:

$$[O(\mathbf{k})]^{\alpha,\alpha'}_{(m\sigma),(m'\sigma')} = \sum_{\nu=\nu_{\min}(\mathbf{k})}^{\nu_{\max}(\mathbf{k})} \widetilde{P}^{\alpha,\sigma}_{\ell m,\nu}(\mathbf{k}) \widetilde{P}^{\alpha',\sigma'*}_{\ell m',\nu}(\mathbf{k}), \quad (15)$$

leading to the final projectors:

$$P^{\alpha,\sigma}_{\ell m,\nu}(\mathbf{k}) = \sum_{\alpha',m',\sigma'} \{[O(\mathbf{k})]^{-1/2}\}^{\alpha,\alpha'}_{(m\sigma),(m'\sigma')} \widetilde{P}^{\alpha',\sigma'}_{\ell m'\nu}(\mathbf{k}), \quad (16)$$

which are then further transformed into a j,m_j basis as described above (see equation (9)).

3.3. Effective local Coulomb interactions from first principles

Hubbard interactions U—obtained as the static ($\omega = 0$) limit of the on-site matrix element $\langle |W^{\mathrm{partial}}| \rangle$ within the 'constrained random phase approximation' (cRPA)—have by now been obtained for a variety of systems, ranging from transition metals [211] to oxides [204, 212–215], pnictides [181, 186, 216, 217], f-electron elements [218] and compounds [187], to surface systems [219], and several implementations within different electronic structure codes and basis sets have been done, e.g. within linearized muffin tin orbitals [211, 220], maximally localized Wannier functions [212, 216, 221] (as elaborated in [222]), or localized orbitals constructed from projected atomic orbitals [204]. The implementation into the framework of the Wien2k package [204] made it possible for Hubbard U's be calculated for the same orbitals as the ones used in subsequent DFT+DMFT calculations, and, to our knowledge, [21] was indeed the first work using in this way consistently calculated Hubbard interactions in a DFT+DMFT calculation. Systematic calculations investigating the basis set dependence for a series of correlated transition metal oxides revealed further interesting trends, depending on the choice of the low-energy subspace. In contrast to common belief until then, Hubbard interactions increase, for example, with the principal quantum number when low-energy effective models encompassing only the t_{2g} orbitals are employed. These trends can be rationalized by two counteracting mechanisms, the increasing extension of the orbitals with increasing principal quantum number and the less efficient screening by oxygen states [204]. We will come back to this point below, in the context of the cRPA calculations for our target compounds.

In the following, we review the specificities involved when determining the Hubbard interactions for our target spin–orbit compounds. We hereby use the same notations as in [204].

We start from the standard Hubbard–Kanamori Hamiltonian H_{int} which allows us to describe the interactions between t_{2g} orbitals within a Hamiltonian restricted to the t_{2g}-space:

$$H_{\mathrm{int}} = \mathcal{U} \sum_{m} n_{m\uparrow} n_{m\downarrow} + \mathcal{U}' \sum_{m<n,\sigma} n_{m\sigma} n_{n\bar{\sigma}} + (\mathcal{U}' - \mathcal{J}) \sum_{m<n,\sigma} n_{m\sigma} n_{n\sigma} - \mathcal{J} \sum_{m<n,\sigma} [c^{\dagger}_{m\sigma} c_{m\bar{\sigma}} c^{\dagger}_{n\bar{\sigma}} c_{n\sigma} + c^{\dagger}_{m\sigma} c^{\dagger}_{m\bar{\sigma}} c_{n\sigma} c_{n\bar{\sigma}}], \quad (17)$$

where $\mathcal{U}$ is the intra-orbital Coulomb repulsion term and $\mathcal{U}'$ ($= \mathcal{U} - 2\mathcal{J}$ with cubic symmetry) the inter-orbital Coulomb interaction which is reduced by Hund's exchange $\mathcal{J}$. (m and n run over the three t_{2g} orbitals and σ stands for the spin).

To draw the link between the cRPA calculations and this model Hamiltonian, the terms $\mathcal{U}$, $\mathcal{U}'$ and $\mathcal{J}$ are understood as the Slater-symmetrized effective interactions in the t_{2g} subspace, related to the Slater integrals F^0, F^2 and F^4 as:

$$\mathcal{U} = F^0 + \frac{4}{49}(F^2 + F^4) \quad \text{and} \quad \mathcal{J} = \frac{3}{49}F^2 + \frac{20}{441}F^4. \quad (18)$$

The last relation $\mathcal{U}' = F^0 - \frac{2}{49}F^2 - \frac{4}{441}F^4$ is redundant since $\mathcal{U}' = \mathcal{U} - 2\mathcal{J}$.

One now transforms H_{int} into the j_{eff} basis using the unitary matrix transformation $\mathcal{S}^{m_j,\sigma}_{j,lm}$. Keeping only density-density terms, H_{int} becomes:

$$H_{\mathrm{int}} = \frac{1}{2} \sum_{j,m_j} \sum_{j',m_{j'}} U^{m_j m_{j'}}_{jj'} n_{j,m_j} n_{j,m_{j'}}. \quad (19)$$

Here, the index j is a shortcut notation for the $j_{\mathrm{eff}} = \{3/2, 1/2\}$ quantum number and $m_j = \{\pm 3/2, \pm 1/2\}$. The reduced interaction matrix $U^{m_j m_{j'}}_{jj'}$ has the following form:

$$U^{m_j m_{j'}}_{jj'} = U^{\overline{m}_j \overline{m}_{j'}}_{jj'} = \left(\begin{array}{c|cc} 0 & \mathcal{U}-2\mathcal{J} & \mathcal{U}-\frac{5}{3}\mathcal{J} \\ \hline \mathcal{U}-2\mathcal{J} & 0 & \mathcal{U}-\frac{7}{3}\mathcal{J} \\ \mathcal{U}-\frac{5}{3}\mathcal{J} & \mathcal{U}-\frac{7}{3}\mathcal{J} & 0 \end{array}\right)$$

$$U^{m_j \overline{m}_{j'}}_{jj'} = U^{\overline{m}_j m_{j'}}_{jj'} = \left(\begin{array}{c|cc} \mathcal{U}-\frac{4}{3}\mathcal{J} & \mathcal{U}-\frac{8}{3}\mathcal{J} & \mathcal{U}-\frac{8}{3}\mathcal{J} \\ \hline \mathcal{U}-\frac{8}{3}\mathcal{J} & \mathcal{U}-\mathcal{J} & \mathcal{U}-\frac{7}{3}\mathcal{J} \\ \mathcal{U}-\frac{8}{3}\mathcal{J} & \mathcal{U}-\frac{7}{3}\mathcal{J} & \mathcal{U}-\mathcal{J} \end{array}\right) \quad (20)$$

We use the standard convention that $\overline{m}_j$ denotes $-m_j$, as is usually done for spin degree of freedom. The ordering of the orbitals $|j, |m_j|\rangle$ is: $|1/2, 1/2\rangle, |3/2, 1/2\rangle, |3/2, 3/2\rangle$, $j_{\mathrm{eff}} = 1/2$ and $j_{\mathrm{eff}} = 3/2$ blocks are emphasized to ease the reading of the matrices.

3.4. Technicalities of the DMFT calculation

For the solution of the quantum impurity problem we apply the continuous-time quantum Monte Carlo method (CTQMC) in the strong-coupling formulation [223]. We are able to perform calculations at room temperature ($\beta = 1/k_B T = 40\,\mathrm{eV}^{-1}$) with reasonable numerical effort. In our calculations, we typically use around 16×10^6 Monte Carlo sweeps and 28 **k**-points in the irreducible Brillouin zone.

Since the CTQMC solver computes the Green's function on the imaginary-time axis, an analytic continuation is needed in order to obtain results on the real-frequency axis. A continuation of the impurity self-energy using a stochastic version of the maximum entropy method [224] yields real and imaginary parts of the retarded self-energy. From those, we calculate the momentum-resolved spectral function $A(\mathbf{k}, \omega)$ using partial projectors introduced in the appendix.

During the calculations we use the fully localized limit (FLL) expression for the double-counting:

$$\Sigma^{\mathrm{dc}}_{j,j'} = \left[\mathcal{U}(N_c - \frac{1}{2}) - \mathcal{J}(\frac{1}{2}N_c - \frac{1}{2})\right]\delta_{jj'}, \qquad (21)$$

where j and j' run over the j_{eff} states and N_c is the total occupancy of the orbitals. (Since each orbital is doubly degenerate in m_j, $N_c/2$ is used in the term containing J). Moreover, we neglect the off-diagonal terms in the local Green's functions (particularly, we neglect the term between the $j_{\mathrm{eff}} = 1/2$ and the $j_{\mathrm{eff}} = 3/2$ $|m_j| = 1/2$ which we checked to be two orders of magnitude smaller than the diagonal terms, in the chosen basis).

4. Electronic structure of Sr_2IrO_4 and Sr_2RhO_4

4.1. Electronic structure of Sr_2IrO_4 and Sr_2RhO_4 within DFT-LDA

The Kohn–Sham band structures of Sr_2IrO_4 and Sr_2RhO_4 within the local density approximation and in the presence of spin–orbit coupling (LDA + SO) are represented in figures 4(d) and (e). For Sr_2IrO_4, we use the lattice parameters measured at 295 K in [225], and for Sr_2RhO_4 those measured at 300 K in [226].

The LDA + SO band structures for Sr_2IrO_4 and Sr_2RhO_4 are very similar, as a consequence of both the structural similarity and the key role of spin–orbit coupling in these compounds. The e_g-states ($d_{x^2-y^2}$ in red and $d_{3z^2-r^2}$ in yellow) start at about 1–1.5 eV, and are fully separated from the t_{2g}-manifold which lies around the Fermi level and overlaps at lower energies with the oxygen 2p-states (black). Given the t^5_{2g} filling and the four-atom unit cell of both compounds, a metallic solution is obtained within LDA for both Sr_2RhO_4 and Sr_2IrO_4—at variance with experiments for Sr_2IrO_4. Among the t_{2g}-manifold (in green), only the four highest-lying bands, highlighted in blue, cross the Fermi level: this is suggestive of the existence of a separated half-filled $j_{\mathrm{eff}} = 1/2$ -derived band, which—within a four-atom unit cell—corresponds to a quartet of bands at each k-point. We stress, however, that the true picture is much more subtle: in fact, $j_{\mathrm{eff}} = 1/2$ and

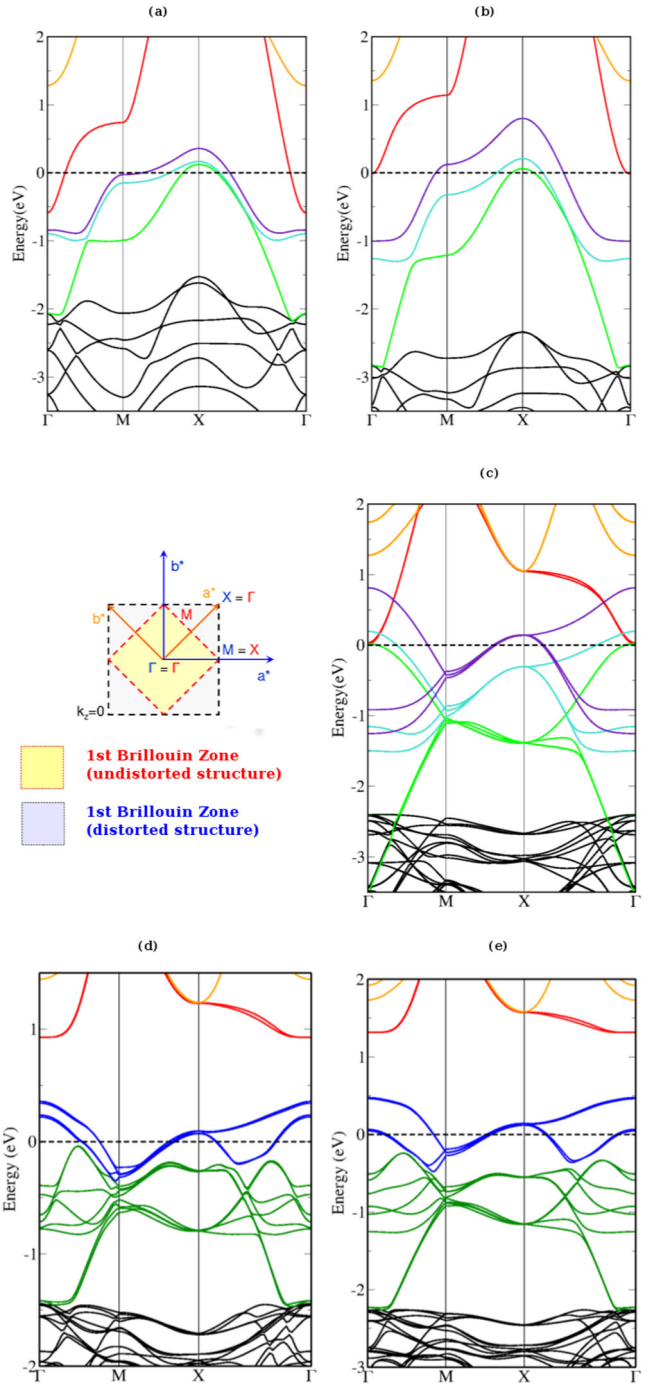

Figure 4. Kohn–Sham band structures within LDA + SO of Sr_2RhO_4 and Sr_2IrO_4 assuming that they crystallize without distortions in a K_2NiF_4 structure ((a)–(b)), of Sr_2IrO_4 in a supercell containing four 'undistorted' unit-cells (c) and of 'real' Sr_2RhO_4 and Sr_2IrO_4 ((d)–(e)). The reduction of the first Brillouin zone, when the crystal symmetry is lowered, is also shown. The e_g states are plotted in yellow ($d_{3z^2-r^2}$) and red ($d_{x^2-y^2}$) while the O-2p states are in black. In the t_{2g} manifold, the $j_{\mathrm{eff}} = 1/2$ are plotted in purple, the $j_{\mathrm{eff}} = 3/2$ $m_j = 3/2$ in light blue and the $j_{\mathrm{eff}} = 3/2$ $m_j = 1/2$ in green.

$j_{\mathrm{eff}} = 3/2$ overlap (see the band structure between the Γ and the M-point for instance) and the identification of the upper four bands as the $j_{\mathrm{eff}} = 1/2$ states is too simplistic. We will come back to this point below.

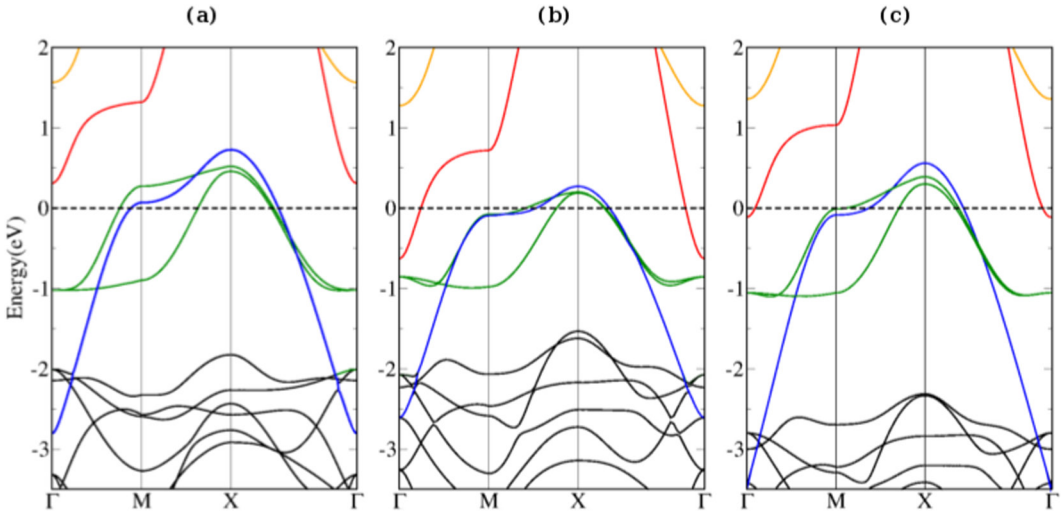

Figure 5. Kohn–Sham band structures of Sr_2RuO_4 (a), Sr_2RhO_4 (b) and Sr_2IrO_4 (c) within LDA (and without spin–orbit coupling), artificially assuming that both Sr_2RhO_4 and Sr_2IrO_4 crystallize in the same K_2NiF_4 structure as their Ru-counterpart. For Sr_2RuO_4, we use the lattice parameters at 300 K given in [227]. The t_{2g}-dominated bands are plotted in green (d_{xy}) and blue (d_{xz} and d_{yz}) while the e_g bands are in red ($d_{x^2-y^2}$) and yellow ($d_{3z^2-r^2}$), and the O-2p states are plotted in black.

To get a better understanding of the Kohn–Sham band structures of Sr_2RhO_4 and Sr_2IrO_4, we study artificial compounds where both the structural distortions and the spin–orbit coupling have been switched off. Figures 5(b) and (c) depict the LDA band structure of such 'idealized undistorted Sr_2RhO_4 and Sr_2IrO_4'. Neglecting the rotation of about 10° of their IrO_6 and RhO_6 octahedra around the c-axis leads to a K_2NiF_4-type crystal structure, like in Sr_2RuO_4, the well-known LDA band structure of which is plotted in figure 5(a).

The similarity of the three band structures is obvious. Around the Fermi level, one distinguishes the three t_{2g} bands. The d_{xy}-band (green) reaches out to lower energies and overlaps with the oxygen 2p-states (black). The e_g-states ($d_{x^2-y^2}$ in red and $d_{3z^2-r^2}$ yellow), higher in energy, cut the Fermi level in both Sr_2IrO_4 and Sr_2RhO_4 due the additional electron remaining in the d-manifold, contrary to Sr_2RuO_4, which has actually a mere t_{2g}^4-filling. The larger extension of the 5d orbitals (see figure 1) explains the wider bandwidth observed for Sr_2IrO_4 in comparison to Sr_2RhO_4: the d_{xy} band reaches the value of -3.5 eV in Γ, while it remains above -3 eV for the 4d counterparts. Another consequence of this wider extension is the stronger hybridization between the 5d states with the oxygen p-states, which are located 1 eV lower in energy in Sr_2IrO_4 than in the 4d-TMOs.

Re-introducing the effects of the spin–orbit coupling in Sr_2RhO_4 and Sr_2IrO_4 (but without considering the structural distortions) modifies these Kohn–Sham band structures to those shown in figures 4(a) and (b). The t_{2g} bands are the most affected, while the e_g bands are slightly shifted as a consequence of the topological change in the t_{2g} manifold. A detailed study of the character of these band structures confirms the decoupling between e_g and t_{2g} states (see also [19, 20]). The cubic crystal field at stake in these compounds is indeed much larger than the energy scale associated with the spin–orbit coupling of about $\zeta_{SO} \approx 0.4$ eV and $\zeta_{SO} \approx 0.2$ eV for Sr_2IrO_4 and Sr_2RhO_4 respectively.

The j_{eff} picture is thus justified in both Sr_2IrO_4 and Sr_2RhO_4: the t_{2g} orbitals split into a quartet of $j_{\text{eff}} = 3/2$ states and a higher lying doublet $j_{\text{eff}} = 1/2$ (see figure 2). Each state is doubly degenerate in $\pm m_j$, since we observe the system in its paramagnetic phase at room temperature and the crystal structure has a center of inversion. Therefore we still refer to them as the '$j_{\text{eff}} = 1/2$ band' and the two '$j_{\text{eff}} = 3/2$ bands' in the following. The three j_{eff} bands can easily be identified: the $j_{\text{eff}} = 1/2$ one (light green) lies above the two $j_{\text{eff}} = 3/2$ ones ($m_j = 3/2$ in light blue and $m_j = 1/2$ in violet). The three j_{eff} bands are well-separated all along the **k**-path, and more generally in the whole Brillouin zone. Since the spin–orbit coupling is half the size in Sr_2RhO_4, the splitting between the j_{eff} bands is reduced by a factor of 2, as one can see, for instance, at X or Γ.

To draw the link between the 'undistorted' band structures and the realistic ones, we plot in figure 4(c) the LDA + SO band structure of the *undistorted* Sr_2IrO_4 in a supercell containing four unit cells. Each band is now folded four times and we provide a scheme of the two first Brillouin zones in the $\mathbf{k}_z = 0$ plane to understand the correspondence between the high-symmetry points of each structure.

Comparing figures 4(c) and (e) highlights the key role of the structural distortion in Sr_2IrO_4: a hybridisation between two neighboring Ir d_{xy} and $d_{x^2-y^2}$ orbitals via the in-plane oxygens is now allowed and pushes the t_{2g} and e_g bands apart. Another consequence of the distortions is the general narrowing of the j_{eff} bandwidth, which is of crucial importance in driving the compound insulation, as we will see below.

Finally, comparing figures 4(c) and (e) gives more insight into the nature of the four highest-lying bands (blue) of figure 4(e). Along the $M - -X$ direction, each quartet of the j_{eff} bands remain well-separated, $j_{\text{eff}} = 1/2$ and $j_{\text{eff}} = 3/2$ overlap in the other direction $\Gamma - M$ and $M - X$. As a result, the $j_{\text{eff}} = 3/2$ bands cross the Fermi-level closest to the

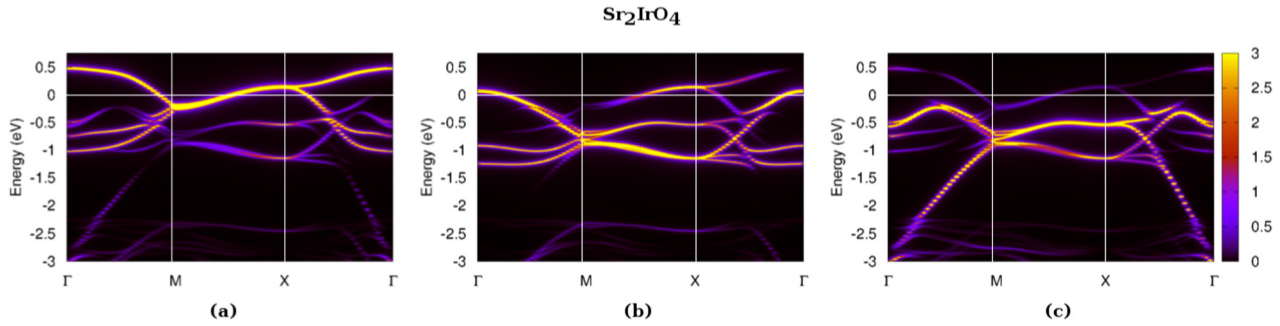

Figure 6. LDA + SO band structure of Sr_2IrO_4, projected on the $j_{\text{eff}} = 1/2$ (a), $j_{\text{eff}} = 3/2\,|m_j| = 3/2$ (b), and $j_{\text{eff}} = 3/2\,|m_j| = 1/2$ (c) spin-orbitals.

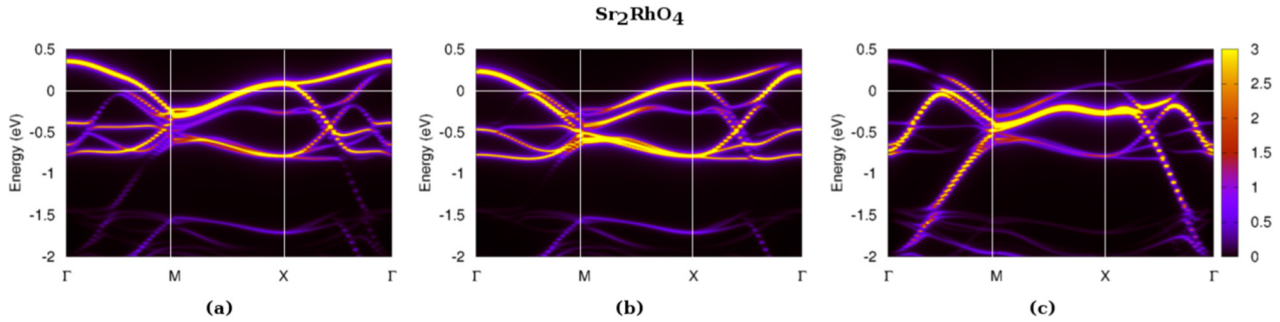

Figure 7. LDA + SO band structure of Sr_2RhO_4, projected on the $j_{\text{eff}} = 1/2$ (a), $j_{\text{eff}} = 3/2\,|m_j| = 3/2$ (b), and $j_{\text{eff}} = 3/2\,|m_j| = 1/2$ (c) spin-orbitals.

Γ-point, while the other crossings are due to the $j_{\text{eff}} = 1/2$ bands. The identification of the upper four bands in Sr_2IrO_4 as 'pure' $j_{\text{eff}} = 1/2$ states is thus too simplistic, implying the need for a Hamiltonian containing more than one orbital in a realistic calculation.

The same mechanisms are important in Sr_2RhO_4 even though we do not display the orbital characters here: the four highest-lying bands, highlighted in blue in figure 4(d) exhibit a mixed character of type $j_{\text{eff}} = 1/2$ and $j_{\text{eff}} = 3/2$. Moreover, thanks to the distortions which allow the opening of a gap between t_{2g} and e_g bands, the LDA + SO Fermi surface becomes qualitatively similar to the experimental one; as shown in figure 8(a), they both contain three closed contours: a circular hole-like α-pocket around Γ, a lens-shaped electron pocket β_M and a square-shaped electron pockets β_X. However, the striking discrepancies in the size of the pockets point out a subtle deficiency in the LDA for Sr_2RhO_4 [19, 20].

4.2. Wannier functions

We have derived the Wannier functions associated with the j_{eff} manifold for both Sr_2IrO_4 and Sr_2RhO_4, using the framework introduced in section 3.1. Because of the mixed character of the four bands that cross the Fermi level in Sr_2IrO_4 and Sr_2RhO_4, the local effective atomic problem used in the DMFT cycle must contain the three j_{eff} orbitals and thus accommodate five electrons. We construct Wannier functions for the j_{eff} orbitals from the LDA + SO band structure of Sr_2IrO_4 and Sr_2RhO_4, using an energy window $[-3.0, 0.5]$ eV for Sr_2IrO_4 and an energy window $[-2.67; 0.37]$ eV for Sr_2RhO_4.

Table 4. Coefficients and occupation (within LDA + SO) of the j_{eff} Wannier orbitals in 'undistorted' Sr_2IrO_4. The discrepancy between these coefficients and those given in equations (1) and (2) are due to the small elongation of the octahedra along the c-axis.

'Undistorted' Sr_2IrO_4	$\left\vert\frac{1}{2}, \pm\frac{1}{2}\right\rangle$	$\left\vert\frac{3}{2}, \pm\frac{1}{2}\right\rangle$	$\left\vert\frac{3}{2}, \pm\frac{3}{2}\right\rangle$
$\vert d_{xy}\uparrow\downarrow\rangle$	± 0.6605	$+0.7508$	0
$\vert d_{xz}\uparrow\downarrow\rangle$	$\pm 0.5309\,i$	$-0.4670\,i$	$-0.7071\,i$
$\vert d_{yz}\uparrow\downarrow\rangle$	$+0.5309$	∓ 0.4670	∓ 0.7071
Occupation (LDA + SO)	1.20	1.92	1.86

Figures 6 and 7 depict the projection of these Wannier functions on the LDA + SO band structure. The similarities between figures 6 and 4(c) are numerous, thus confirming our previous band character analysis. Table 5 gives the decomposition of these local Wannier functions on the t_{2g} manifold and their respective occupation.

To obtain deeper insights into the nature of these Wannier orbitals, table 4 gives the coefficients of the local Wannier orbitals obtained from the LDA + SO band structure of 'undistorted' Sr_2IrO_4 using an energy window $[-3.5, 0.8]$ eV. The results agree well with the standard j_{eff} picture (see equations (1) and (2)) in both modulus and phase. Discrepancies are mostly due to the elongation of the IrO_6 along the c-axis, which introduces an additional tetragonal field between the t_{2g} states. This effect also explains the lifting of the degeneracy of the two $j_{\text{eff}} = 3/2$ ($m_j = \pm 1/2$ and $m_j = \pm 3/2$) states and implies the reason why the $j_{\text{eff}} = 1/2$ is slightly more than half-filled.

Table 5. Modulus of the coefficients of the $j_{\rm eff}$ Wannier orbitals in Sr_2IrO_4 and Sr_2RhO_4. The occupation within LDA + SO and the charge within LDA + SO+DMFT of each atomic Wannier orbital are also provided, showing how electronic correlations enhance the spin–orbital polarization.

	Sr_2IrO_4			Sr_2RhO_4		
Wannier orbitals	$\left\|\frac{1}{2},\pm\frac{1}{2}\right\rangle$	$\left\|\frac{3}{2},\pm\frac{1}{2}\right\rangle$	$\left\|\frac{3}{2},\pm\frac{3}{2}\right\rangle$	$\left\|\frac{1}{2},\pm\frac{1}{2}\right\rangle$	$\left\|\frac{3}{2},\pm\frac{1}{2}\right\rangle$	$\left\|\frac{3}{2},\pm\frac{3}{2}\right\rangle$
$\|d_{x^2-y^2}\uparrow\downarrow\rangle$	0.0388	0.0766	0	0.0100	0.0302	0
$\|d_{xy}\uparrow\downarrow\rangle$	0.4499	0.8889	0	0.3153	0.9485	0
$\|d_{xz}\uparrow\downarrow\rangle$	0.6309	0.3193	0.7071	0.6710	0.2231	0.7071
$\|d_{yz}\uparrow\downarrow\rangle$	0.6309	0.3193	0.7071	0.6710	0.2231	0.7071
occupation (LDA + SO)	1.16	1.98	1.84	1.42	1.96	1.64
charge (LDA + SO+DMFT)	1.02	2.00	1.98	1.26	1.98	1.76

Because of the hybridization between the d_{xy} and $d_{x^2-y^2}$ orbitals in the distorted structures, we had to define in practice 'effective $j_{\rm eff} = 1/2$ and $j_{\rm eff} = 3/2$ $|m_j| = 1/2$ states', which remain close to the atomic $j_{\rm eff}$ picture but take into account a small amount of $d_{x^2-y^2}$ character (see table 5). The coefficients have been calculated such that the density matrix of the local atomic problem is the closest possible to the diagonal form[4]. In addition to the hybridization, the construction of the 'effective $j_{\rm eff}$' also takes into account the tetragonal crystal field due to the elongation of the octahedra in each crystal structure; this explains the discrepancies with the standard coefficients given in equations (1) and (2). We note that the coefficients obtained for the $j_{\rm eff} = 1/2$ state of Sr_2IrO_4 are equivalent to those obtained in the AF phase in [139].

Finally, comparing the occupation of the orbitals in tables 4 and 5 highlights again the role of the hybridisation between the d_{xy} and $d_{x^2-y^2}$ orbitals which pushes the band $j_{\rm eff} = 3/2$ $|m_j| = 1/2$ further below the Fermi level close to Γ. As a result, the four bands that cross the Fermi level are formed only by the $j_{\rm eff} = 1/2$ and $j_{\rm eff} = 3/2$ $|m_j| = 3/2$ orbitals and the $j_{\rm eff} = 1/2$ tend to be close to half-filling. Similar conclusions were drawn for the AF phase within a variational cluster approximation (VCA) approach in [140]. Similar conclusions hold for Sr_2RhO_4.

4.3. Effective Hubbard interactions from cRPA

After defining the $j_{\rm eff}$ Wannier orbitals, we evaluate the local Coulomb interaction in the effective atomic problem within cRPA [204, 211], as explained in section 3.3. For reasons of computational resources, the cRPA calculations were performed in the case without distortions (without the rotations of the octahedra, hence considering only one formula-unit in a unit-cell) and without SOC. To mimic the effect of the distortions, the e_g states are shifted up to their energetic position in the presence of distortions. We find $\mathcal{U} = 2.54$ eV and $\mathcal{J} = 0.23$ eV for Sr_2IrO_4 and $\mathcal{U} = 1.94$ eV and $\mathcal{J} = 0.23$ eV for Sr_2RhO_4. These parameters lead to the following local interaction matrices for Sr_2IrO_4:

$$U_{jj'}^{m_j m_{j'}} = \left(\begin{array}{c|cc} 0 & 2.08 & 2.21 \\ \hline 2.08 & 0 & 1.93 \\ 2.21 & 1.93 & 0 \end{array}\right) \tag{22}$$

$$U_{jj'}^{m_j \overline{m}_{j'}} = \left(\begin{array}{c|cc} 2.25 & 1.98 & 1.90 \\ \hline 1.98 & 2.38 & 2.03 \\ 1.90 & 2.03 & 2.31 \end{array}\right) \tag{23}$$

and for Sr_2RhO_4:

$$U_{jj'}^{m_j m_{j'}} = \left(\begin{array}{c|cc} 0 & 1.48 & 1.66 \\ \hline 1.48 & 0 & 1.29 \\ 1.66 & 1.29 & 0 \end{array}\right) \tag{24}$$

$$U_{jj'}^{m_j \overline{m}_{j'}} = \left(\begin{array}{c|cc} 1.67 & 1.32 & 1.27 \\ \hline 1.32 & 1.86 & 1.46 \\ 1.27 & 1.46 & 1.71 \end{array}\right) \tag{25}$$

where the values are in eV and the ordering of the $|j, |m_j|\rangle$ orbitals is: $|1/2, 1/2\rangle$, $|3/2, 1/2\rangle$, $|3/2, 3/2\rangle$ and $\overline{m}_j$ denotes $-m_j$. We remind the reader that $U_{jj'}^{m_j m_{j'}} = U_{jj'}^{\overline{m}_j \overline{m}_{j'}}$ and $U_{jj'}^{m_j \overline{m}_{j'}} = U_{jj'}^{\overline{m}_j m_{j'}}$. Since we have used 'effective $j_{\rm eff}$' Wannier orbitals instead of the standard definition given in equations (1) and (2), some discrepancies with the formulae given in equation (20) and in [22] can be observed. Contrary to common belief, the Hubbard interactions are smaller in the 4*d*-TMO than in its 5*d*-counterpart. This might seem counterintuitive at first sight, since the 5*d*-orbitals are more extended than the 4*d* ones, but finds its explanation in more efficient screening in the 4*d* material: As shown in figures 4(d) and (e), the hybridization between the Rh-4*d* states and the O-2*p* is weaker in Sr_2RhO_4 than in Sr_2IrO_4. Correspondingly, the energetic position of the O-2*p* bands is closer to the Fermi level by about 1 eV, and as a result, the Coulomb interactions are screened more efficiently in Sr_2RhO_4 than in Sr_2IrO_4, explaining the observed trend.

4.4. Correlated electronic structure of Sr_2IrO_4 and Sr_2RhO_4

DFT+DMFT calculations following the procedure described in section 3.1 indeed find an insulating solution for Sr_2IrO_4 and a correlated metal for Sr_2RhO_4 [21], in agreement with experiment. The difference in the metallic versus insulating

[4] With the obtained coefficients, the off-diagonal terms remaining in the local Green's functions between the $j_{\rm eff} = 1/2$ and $j_{\rm eff} = 3/2$ $|m_j| = 1/2$ are smaller than 0.05. In practice, the coefficients were chosen to be real. This can be done in the local problem since only density-density terms were kept for the interaction terms and off-diagonal terms of the density matrix were neglected.

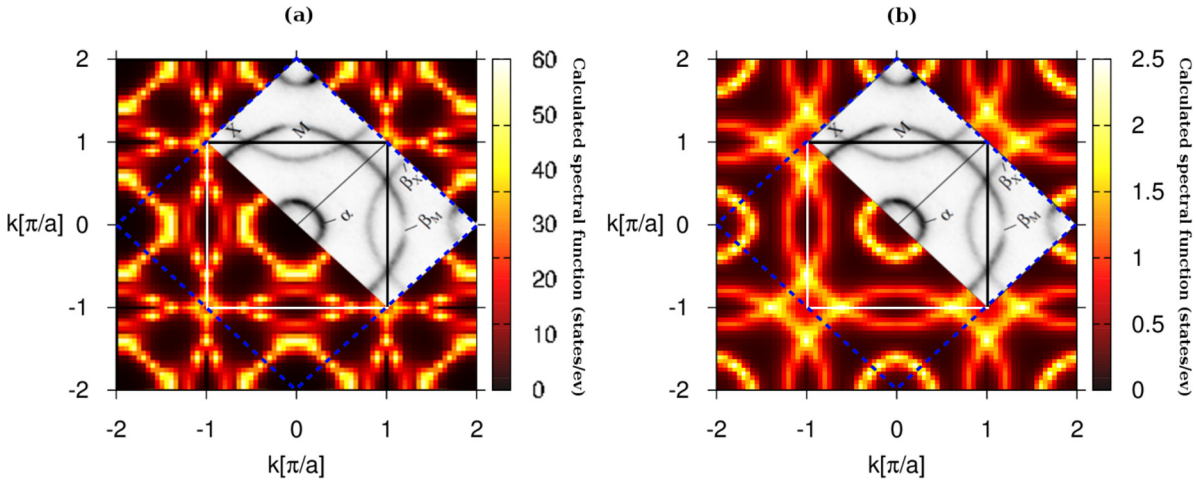

Figure 8. Calculated Fermi surface of Sr_2RhO_4 in the $\mathbf{k}_z = 0$ plane within LDA + SO (left panel) and LDA + SO+DMFT (right panel). Superimposed is the experimentally measured Fermi surface. Adapted with permission from [120]. Copyright 2006 by the American Physical Society.

Table 6. Comparison of the Fermi surface (FS) parameters evaluated within LDA + SO, within LDA + SO+DMFT and ARPES [120]. For each α, β_X and β_M pocket, the FS volume A is defined as a percentage of the two-dimensional BZ volume (using the experimental lattice parameters ($a = 5.45$ Å)). The Fermi velocity $\hbar\overline{v_F}$ is obtained from the slope of the band dispersion at the Fermi level. The cyclotron mass m^*/m_e is calculated using the same method as described in [120]: $m^*\overline{v_F} = \hbar\sqrt{A/\pi}$.

	α			β_X			β_M		
	LDA	DMFT	Exp.	LDA	DMFT	Exp.	LDA	DMFT	Exp.
FS volume A (% BZ)	18.4	10.1	6.1(4)	4.5	6.2	8.1(5)	10.0	7.6	7.4(4)
$\hbar\overline{v_F}$ (eV · Å)	1.252	0.645	0.41(4)	1.260	0.674	0.55(6)	1.260	0.674	0.61(6)
m^* (m_e)	1.70	2.44	3.0(3)	0.83	1.83	2.6(3)	1.24	2.02	2.2(2)

nature of Sr_2RhO_4 and Sr_2IrO_4 can be traced back to the different spin–orbital polarization in the three j_{eff} orbitals, which is enhanced by Coulomb correlations.

The occupations of the j_{eff} Wannier orbitals within LDA + SO and LDA + SO+DMFT are provided in table 5. In Sr_2IrO_4, one detects a considerable spin–orbital polarization already at the LDA + SO level: the four $j_{\text{eff}} = 3/2$ states are almost filled with $n_{3/2,|1/2|} = 1.98$ and $n_{3/2,|3/2|} = 1.84$ while the $j_{\text{eff}} = 1/2$ states thus slightly exceed half-filling with $n_{1/2} = 1.16$ (as in the 'ideal undistorted' case). Taking into account Coulomb correlations within DMFT opens a gap of about 0.26 eV [21] and enhances the spin–orbital polarization, such as to fill the $j_{\text{eff}} = 3/2$ states entirely, leading to a half-filled $j_{\text{eff}} = 1/2$ state. This is thus the celebrated '$j_{\text{eff}} = 1/2$ -picture' [16], which comes out here as a result of the calculations, rather than being an input as in most model Hamiltonian calculations.

A different picture emerges for Sr_2RhO_4 according to table 5: while the spin–orbital occupations display some polarization at the LDA + SO level, the smaller SOC—and thus the smaller effective splitting between the j_{eff} bands—leads to a picture where only the $j_{\text{eff}} = 3/2\,|m_j| = 1/2$ state is entirely filled, while both $j_{\text{eff}} = 3/2\,|m_j| = 3/2$ and $j_{\text{eff}} = 1/2$ live at the Fermi level. This spin–orbital polarization is enhanced by Coulomb correlations—just as in Sr_2IrO_4—but this enhancement is not enough to fill both $j_{\text{eff}} = 3/2$ states entirely and obtain a half-filled $j_{\text{eff}} = 1/2$ state. The higher effective degeneracy, together with the smaller value of $\mathcal{U}$, eventually leaves Sr_2RhO_4 metallic.

4.5. Spectral properties of Sr_2RhO_4: theory vs. experiment

We now turn to the calculated spectral function of the spin–orbital correlated metal Sr_2RhO_4 that we analyze in comparison to experiment.

Figure 8 depicts the Fermi surface of Sr_2RhO_4 within LDA + SO (left panel) and LDA + SO+DMFT (right panel) in the $\mathbf{k}_z = 0$ plane, on which we superimpose the experimental measurement from [120]. Table 6 gives more quantitative insight to ease the comparison between the different topologies. All three Fermi surfaces, the two theoretical ones and the experimental one, are *qualitatively* similar with three closed contours: a circular hole-like α-pocket around Γ, a lens-shaped electron pocket β_M and a square-shaped electron pockets β_X. These two structures merge in the undistorted tetragonal zone (dashed blue line in figure 8) to a large electron-like pocket β.

Comparing figures 8(a) and (b) highlights the key role of electronic correlations: they decrease the radius of the α pocket from 0.26–0.29 Å^{-1} to 0.21 Å^{-1} and decrease the radius of the large β pocket from 0.69–0.72 Å^{-1} to 0.67–0.70 Å^{-1}, thus enlarging the β_M and β_X pockets such that their volumes are well-reproduced within LDA + SO+DMFT (see table 6). As a result, the agreement between LDA + SO+DMFT data and the experimental measurements becomes quantitatively excellent.

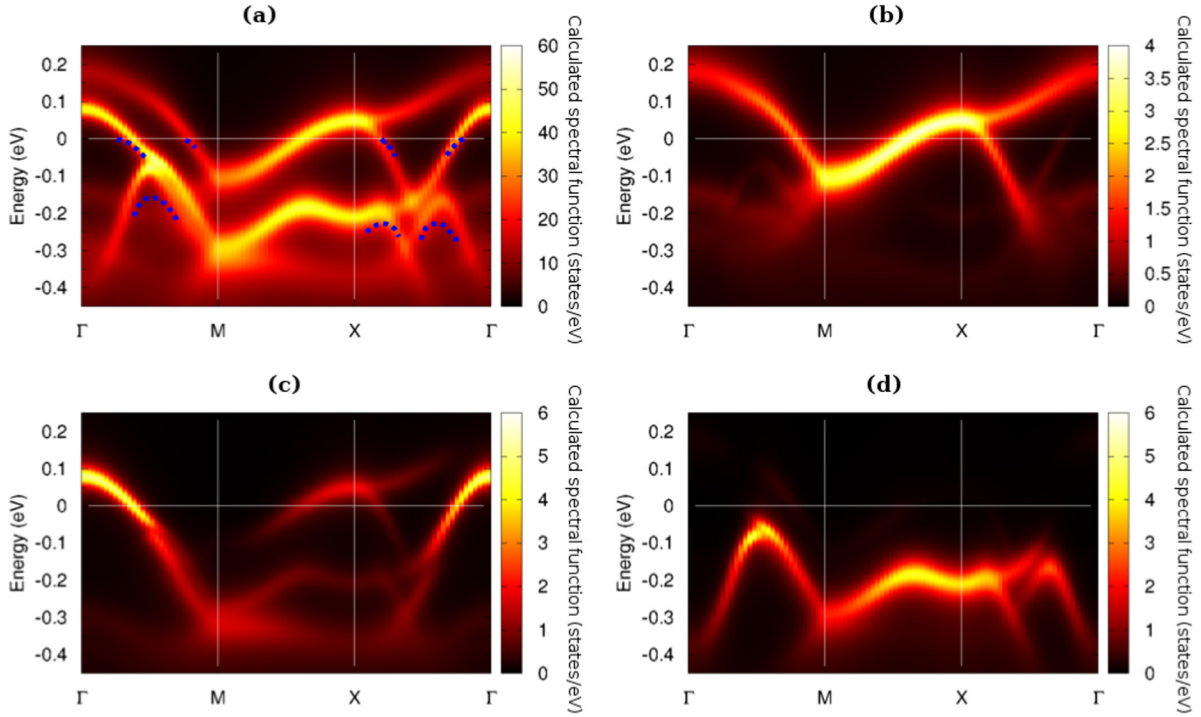

Figure 9. Calculated momentum-resolved spectral function of Sr_2RhO_4 within LDA+DMFT (a) and its orbital-resolved versions for the $j_{\rm eff} = 1/2$ states (b), the $j_{\rm eff} = 3/2\,|m_j| = 3/2$ (c) and the completely-filled $j_{\rm eff} = 3/2\,|m_j| = 1/2$ (d). The dashed blue line on panel (a) is the reproduction of the ARPES structure from [121].

To go further in the analysis, figure 9 depicts the momentum-resolved spectral function, as well as its orbital-resolved version. The completely filled $j_{\rm eff} = 3/2$ $|m_j| = 1/2$ state is visible (panel (d)), as well as the partially filled character of the $j_{\rm eff} = 3/2$ $|m_j| = 3/2$ (panel (c)) and $j_{\rm eff} = 1/2$ states (panel (b)). A detailed comparison with angle-resolved photoemission data from [121] (blue dashed line on the figure) shows that the band dispersion around the Fermi level is well-reproduced, while some discrepancies are observed for the structures experimentally observed along $\Gamma - X$ and $\Gamma - M$ at lower energy. These features, reminiscent of the $j_{\rm eff} = 3/2$ $|m_j| = 1/2$ bands, are indeed about 0.05 eV higher in energy in our calculated spectral function.

From figures 9(b) and (c), one observes that the Fermi level is crossed by the renormalized $j_{\rm eff} = 3/2$ $|m_j| = 3/2$ band at 0.20 Å^{-1} along $\Gamma - X$ and at 0.21 Å^{-1} along $\Gamma - M$, while the renormalized $j_{\rm eff} = 1/2$ band is responsible for all other crossings. This allows us to label the hole-like α-pocket as being of $j_{\rm eff} = 3/2\,|m_j| = 3/2$ type, whereas the two other pockets β_M and β_X are mostly of type $j_{\rm eff} = 1/2$. Using the quasiparticle weight of each state ($Z_{1/2} = 0.535$ and $Z_{3/2,|3/2|} = 0.675$), we evaluate the Fermi velocity at each crossing along the path [$\Gamma MX\Gamma$]: we find a huge variation in the values depending on $\mathbf{k}$ and give in table 6 their mean value over the Brillouin zone. Finally, using the same method as described in [120], we evaluate the cyclotron mass m^*/m_e based on the approximate formula used there: $m^*\overline{v_{\rm F}} = \hbar\sqrt{A/\pi}$. The DMFT results shown in table 6 show a substantial improvement over DFT when compared to experiments.

5. The effective orbital degeneracy as a key quantity determining the correlation strength

In section 4.4, we have identified the spin–orbital polarization as a key factor in explaining the different behavior of Sr_2RhO_4 and Sr_2IrO_4.

In Sr_2IrO_4, Coulomb correlations enhance the spin–orbital polarization, such as to fill the $j_{\rm eff} = 3/2$ states entirely, leading to a half-filled $j_{\rm eff} = 1/2$ one-band picture, while in Sr_2RhO_4 the final situation is an effective two-orbital system containing three electrons. This situation is akin to correlation-induced enhancements of orbital polarization also observed in other transition metal oxides. In the distorted $3d^1$ perovskites $LaTiO_3$ and $YTiO_3$, for example, it was argued [10] that the interplay of structural distortions and Coulomb correlations leads to a suppression of orbital fluctuations in the t_{2g}-manifold, favoring a particular orbital composition selected by crystal and ligand field effects. At the LDA level, 0.45 [0.88] electrons are found in this particular orbital in $LaTiO_3$ [$YTiO_3$], while Coulomb correlations as described by LDA+DMFT lead to an occupation of 0.88 [0.96] electrons.

In these systems, this reduction of effective orbital degeneracy was shown to be key to their insulating nature since the critical interaction strength needed to localize the single electron is thus effectively determined by the one of a single-orbital system, instead of the one of a three-fold degenerate t_{2g}-manifold. Within DMFT, the critical Hubbard interaction scales with the square-root of the orbital degeneracy N for the lower critical interaction of the phase coexistence region of the first order Mott transition, while the upper critical interaction varies with N [228].

Localizing electrons in a single-orbital system therefore needs a critical interaction which is smaller by a factor of roughly 3 as compared to the degenerate case. This was demonstrated to be crucial for the difference in behaviors in the series of d^1 compounds $SrVO_3$, $CaVO_3$, $LaTiO_3$, $YTiO_3$, where the former are three-fold degenerate metallic systems, whereas the latter realize the single-orbital Mott state.

The situation in the iridates is analogous with the purely formal difference that one is dealing with a one-hole situation instead of one electron. Furthermore, the strong spin–orbit interaction is instrumental in the suppression of the degeneracy, which is the net result of structural distortions, spin–orbit coupling and Coulomb correlations.

This discussion highlights an important aspect of the physics of transition metal oxides, often neglected when considering band filling and interaction strength only: the *effective orbital degeneracy* is a crucial tuning parameter for electronic behavior, suggesting that the popular picture distinguishing filling-controlled and bandwidth-controlled Mott transitions [1] should be complemented by a 'third axis' and the notion of degeneracy-controlled Mott behavior.

Crystal and ligand fields, together with spin–orbit coupling and the Coulomb correlations themselves, are the driving forces for establishing a given effective degeneracy. At the level of the calculations, this effective degeneracy is both an outcome of the calculation and a determining factor of the properties of the given compound.

6. Conclusions and perspectives

The common belief about electronic Coulomb correlations being less important in 4d and 5d compounds as compared to 3d transition metal oxides, was overruled by insights into the role of spin–orbit coupling in the insulating behavior of iridates [16] and for the Fermi surface topology of Sr_2RhO_4 [19, 20].

Here, we have reviewed recent work on a first principles many-body description of such effects within a dynamical mean-field framework. We have highlighted the notion of the *effective degeneracy* of the system as a crucial parameter determining the physical properties of a system. The effective degeneracy is the result of a complex interplay of structural distortions, spin–orbit coupling and Coulomb correlations. We have stressed the analogy of the $j_{\rm eff} = 1/2$ Mott insulating picture for Sr_2IrO_4 with the insulating nature of $LaTiO_3$ and $YTiO_3$ in the 'degeneracy-controlled Mott transition' series of d^1 perovskites ($SrVO_3$, $CaVO_3$, $LaTiO_3$, $YTiO_3$) [10].

In Sr_2IrO_4 and Sr_2RhO_4 the difference in degeneracy is itself a consequence of the quantitative aspects of the physics of these two compounds: all three decisive elements—structural distortions, spin–orbit coupling and Hubbard interaction—are smaller in Sr_2RhO_4 than in Sr_2IrO_4 and this quantitative difference in the electronic parameters translates into a qualitative difference in the resulting properties.

We have analyzed in detail the spectral properties of Sr_2RhO_4, a spin–orbit correlated 4d metal where the effective degeneracy is reduced by spin–orbit coupling and correlations but not to the point such as to induce a $j_{\rm eff} = 1/2$ Mott insulator. The calculated spectral properties and Fermi surface are in excellent agreement with experimental data. A detailed analysis of the spectral properties of Sr_2IrO_4 is left for future work.

Acknowledgments

This work was supported by the ERC Consolidator Grant CORRELMAT (grant 617196), the French ANR under project IRIDATES, and IDRIS/GENCI under project t20169313. M.A. is supported by a START program of the Austrian Science Fund (FWF), grant number Y746.

Appendix. Generalized partial Θ-*projectors and spectral function*

In order to calculate quantities for a given atom α and a particular orbital (spin) character j (m_j)—such as the spectral functions $A_j^{m_j\alpha}(\mathbf{k},\omega)$—a set of partial projectors called '*Θ-projectors*' was built. Contrary to the previously introduced Wannier projectors $P_{j,\nu}^{\alpha,m_j}(\mathbf{k})$, their definition is not restricted to the correlated orbitals only. The formalism of these partial projectors was initially introduced in [180] and was extended to the case where spin is not a good quantum number anymore, in [21].

Inside the muffin-tin sphere associated with an atom α, one can write the spin-σ contribution of the eigenstate $\psi_{\mathbf{k}\nu}(\mathbf{r})$ as:

$$\phi^{\sigma}_{\mathbf{k}\nu}(\mathbf{r}) = \sum_{\ell=0}^{\ell_{\max}} \sum_{m=-\ell}^{+\ell} [A^{\nu\alpha}_{\ell m}(\mathbf{k},\sigma)\, u^{\alpha,\sigma}_{\ell m,1}(\mathbf{r}^{\alpha}) + B^{\nu\alpha}_{\ell m}(\mathbf{k},\sigma)\, u^{\alpha,\sigma}_{\ell m,2}(\mathbf{r}^{\alpha}) + C^{\nu\alpha}_{\ell m}(\mathbf{k},\sigma)\, u^{\alpha,\sigma}_{\ell m,3}(\mathbf{r}^{\alpha})],$$

where the basis $\{u^{\alpha,\sigma}_{\ell m,i}\}_{i=\{1,2,3\}}$ is not orthonormalized, as already mentioned in [180]. That is why, to make the calculations easier, one introduces an orthonormal basis set $\{v^{\alpha,\sigma}_{\ell m,j}\}_{\{j=1,2,3\}}$ for each atomic orbital (ℓ, m). These orbitals are defined from the initial basis $\{u^{\alpha,\sigma}_{\ell m,i}\}_{i=\{1,2,3\}}$ as follows:

$$\forall\, i \quad u^{\alpha,\sigma}_{\ell m,i}(\mathbf{r}^{\alpha}) = \sum_{j=1}^{3} c_{ij} v^{\alpha,\sigma}_{\ell m,j}, \tag{A.1}$$

$$\mathbf{C} = \begin{pmatrix} 1 & 0 & \langle u^{\alpha,\sigma}_{\ell m,1} | u^{\alpha,\sigma}_{\ell m,2}\rangle \\ 0 & \langle u^{\alpha,\sigma}_{\ell m,2} | u^{\alpha,\sigma}_{\ell m,2}\rangle & \langle u^{\alpha,\sigma}_{\ell m,2} | u^{\alpha,\sigma}_{\ell m,3}\rangle \\ \langle u^{\alpha,\sigma}_{\ell m,3} | u^{\alpha,\sigma}_{\ell m,1}\rangle & \langle u^{\alpha,\sigma}_{\ell m,3} | u^{\alpha,\sigma}_{\ell m,2}\rangle & 1 \end{pmatrix}^{\frac{1}{2}}. \tag{A.2}$$

We can then rewrite equation (A.1) as:

$$\psi^{\sigma}_{\mathbf{k}\nu}(\mathbf{r}) = \sum_{\ell=0}^{\ell_{\max}} \sum_{m=-\ell}^{+\ell} \sum_{i=1}^{3} \Theta^{\alpha,\sigma}_{\ell m\nu,i}(\mathbf{k}) v^{\alpha,\sigma}_{\ell m,i}(\mathbf{r}^{\alpha}). \tag{A.3}$$

The matrix elements $\Theta^{\alpha,\sigma}_{\ell m\nu,i}(\mathbf{k})$ are the '*Θ-projectors*', which are thus defined by:

$$\Theta^{\alpha,\sigma}_{\ell m\nu,i}(\mathbf{k}) = \langle v^{\alpha,\sigma}_{\ell m,i} | \phi^{\sigma}_{\mathbf{k}\nu}\rangle = A^{\nu\alpha}_{\ell m}(\mathbf{k},\sigma) c_{1i} + B^{\nu\alpha}_{\ell m}(\mathbf{k},\sigma) c_{2i} + C^{\nu\alpha}_{\ell m}(\mathbf{k},\sigma) c_{3i}. \tag{A.4}$$

Contrary to the implementation of [180], there are now a couple of Θ-projectors associated with each band index ν, $\Theta^{\alpha,\sigma}_{\ell m\nu,i}(\mathbf{k})$ with $\sigma = \uparrow, \downarrow$, since spin is not a good quantum number anymore.

We have introduced here the Θ-projectors in the complex spherical harmonics basis. As for the Wannier projectors, it is of course possible to get the Θ-projectors in any desired j,m_j basis:

$$\Theta^{\alpha,m_j}_{j\nu,i}(\mathbf{k}) = \sum_{m,\sigma} \mathcal{S}^{m_j,\sigma}_{j,\ell m} \Theta^{\alpha,\sigma}_{\ell m\nu,i}(\mathbf{k}). \tag{A.5}$$

Finally, the spectral function $A(\mathbf{k},\omega)$, which is defined by:

$$A(\mathbf{k},\omega) = -\frac{1}{\pi}\mathrm{Im}\left[\mathrm{G}(\mathbf{k},\omega)\right], \tag{A.6}$$

is obtained for a given atom α with orbital character (j,m_j) through the following formula:

$$A^{\alpha,m_j}_{j}(\mathbf{k},\omega) = -\frac{1}{\pi}\mathrm{Im}\left[\sum_{\nu\nu'}\sum_{\mathrm{i}=1}^{3} \mathbf{\Theta}^{\alpha,\mathrm{m_j}}_{\mathrm{j}\nu,\mathrm{i}}(\mathbf{k})\mathbf{G}_{\nu\nu'}(\mathbf{k},\omega+\mathrm{i}0^{+})[\mathbf{\Theta}^{\alpha,\mathrm{m_j}}_{\mathrm{j}\nu',\mathrm{i}}(\mathbf{k})]^{*}\right], \tag{A.7}$$

where the band indices ν, ν' run over *both* spin and orbital quantum number.

References

[1] Imada M, Fujimori A and Tokura Y 1998 Metal-insulator transitions *Rev. Mod. Phys.* **70** 1039

[2] Tomczak J M, Casula M, Miyake T and Biermann S 2012 Combined GW and dynamical mean-field theory: dynamical screening effects in transition metal oxides *Europhys. Lett.* **100** 67001

[3] Tomczak J M, Casula M, Miyake T and Biermann S 2014 Asymmetry in band widening and quasiparticle lifetimes in $SrVO_3$: competition between screened exchange and local correlations from combined *gw* and dynamical mean-field theory GW+DMFT *Phys. Rev.* B **90** 165138

[4] Aichhorn M, Biermann S, Miyake T, Georges A and Imada M 2010 Theoretical evidence for strong correlations and incoherent metallic state in FeSe *Phys. Rev.* B **82** 064504

[5] van Roekeghem A, Ayral T, Tomczak J M, Casula M, Xu N, Ding H, Ferrero M, Parcollet O, Jiang H and Biermann S 2014 Dynamical correlations and screened exchange on the experimental bench: spectral properties of the cobalt pnictide $BaCo_2As_2$ *Phys. Rev. Lett.* **113** 266403

[6] van Roekeghem A, Richard P, Shi X, Wu S, Zeng L, Saparov B, Ohtsubo Y, Qian T, Sefat A S, Biermann S and Ding H 2016 Tetragonal and collapsed-tetragonal phases of $CaFe_2As_2$: a view from angle-resolved photoemission and dynamical mean-field theory *Phys. Rev.* B **93** 245139

[7] Razzoli E *et al* 2015 Tuning electronic correlations in transition metal pnictides: chemistry beyond the valence count *Phys. Rev.* B **91** 214502

[8] Ma J-Z *et al* 2014 Correlation-induced self-doping in the iron-pnictide superconductor $Ba_2Ti_2Fe_2As_4O$ *Phys. Rev. Lett.* **113** 266407

[9] Haule K and Kotliar G 2009 Coherence-incoherence crossover in the normal state of iron oxypnictides and importance of Hund's rule coupling *New J. Phys.* **11** 025021

[10] Pavarini E, Biermann S, Poteryaev A, Lichtenstein A I, Georges A and Andersen O K 2004 Mott transition and suppression of orbital fluctuations in orthorhombic $3d^1$ perovskites *Phys. Rev. Lett.* **92** 176403

[11] Poteryaev A I, Tomczak J M, Biermann S, Georges A, Lichtenstein A I, Rubtsov A N, Saha-Dasgupta T and Andersen O K 2007 Enhanced crystal-field splitting and orbital-selective coherence induced by strong correlations in V_2O_3 *Phys. Rev.* B **76** 085127

[12] Tomczak J M, Poteryaev A I and Biermann S 2009 Momentum-resolved spectroscopy of correlated metals: a view from dynamical mean field theory *C. R. Phys.* **10** 537–47

[13] Keller G, Held K, Eyert V, Vollhardt D and Anisimov V I 2004 Electronic structure of paramagnetic v_2o_3: strongly correlated metallic and Mott insulating phase *Phys. Rev.* B **70** 205116

[14] Held K, Keller G, Eyert V, Vollhardt D and Anisimov V I 2001 Mott-Hubbard metal-insulator transition in paramagnetic V_2O_3: an LDA+DMFT(QMC) study *Phys. Rev. Lett.* **86** 5345–8

[15] Kim B J, Ohsumi H, Komesu T, Sakai S, Morita T, Takagi H and Arima T 2009 Phase-sensitive observation of a spin–orbital Mott state in Sr_2IrO_4 *Science* **323** 1329

[16] Kim B J *et al* 2008 Novel $J_{\mathrm{eff}} = 1/2$ Mott state induced by relativistic spin–orbit coupling in Sr_2IrO_4 *Phys. Rev. Lett.* **101** 076402

[17] Rau J G, Lee E K-H and Kee H-Y 2016 Spin–orbit physics giving rise to novel phases in correlated systems: iridates and related materials *Ann. Rev. Condens. Matter Phys.* **7** 195–221

[18] Witczak-Krempa W, Chen G, Kim Y B and Balents L 2014 Correlated quantum phenomena in the strong spin–orbit regime *Ann. Rev. Condens. Matter Phys.* **5** 57–82

[19] Haverkort M W, Elfimov I S, Tjeng L H, Sawatzky G A and Damascelli A 2008 Strong spin–orbit coupling effects on the Fermi surface of Sr_2RuO_4 and Sr_2RhO_4 *Phys. Rev. Lett.* **101** 026406

[20] Liu G-Q, Antonov V N, Jepsen O and Andersen O K 2008 Coulomb-enhanced spin–orbit splitting: the missing piece in the Sr_2RhO_4 puzzle *Phys. Rev. Lett.* **101** 026408

[21] Martins C, Aichhorn M, Vaugier L and Biermann S 2011 Reduced effective spin-orbital degeneracy and spin-orbital ordering in paramagnetic transition-metal oxides: Sr_2IrO_4 versus Sr_2RhO_4 *Phys. Rev. Lett.* **107** 266404

[22] Ahn K-H, Lee K-W and Kuneš J 2015 Doping-dependent bandwidth renormalization and spin–orbit coupling in $(Sr_{1-x}La_x)_2RhO_4$ *J. Phys.: Condens. Matter* **27** 085602

[23] Ando Y 2013 Topological insulator materials *J. Phys. Soc. Japan* **82** 102001

[24] Hasan M Z and Kane C L 2010 *Colloquium*: Topological insulators *Rev. Mod. Phys.* **82** 3045–67

[25] Qi X-L and Zhang S-C 2011 Topological insulators and superconductors *Rev. Mod. Phys.* **83** 1057–110

[26] Perfetti L, Loukakos P A, Lisowski M, Bovensiepen U, Berger H, Biermann S, Cornaglia P S, Georges A and Wolf M 2006 Time evolution of the electronic structure of 1T-TaS_2 through the insulator-metal transition *Phys. Rev. Lett.* **97** 067402

[27] Ritschel T, Trinckauf J, Koepernik K, Büchner B, Zimmermann M V, Berger H, Joe Y I, Abbamonte P and Geck J 2015 Orbital textures and charge density waves in transition metal dichalcogenides *Nat. Phys.* **11** 328

[28] Ma L, Ye C, Yu Y, Lu X F, Niu X, Kim S, Feng D, Tomanek D, Son Y-W, Chen X H and Zhang Y 2016 A metallic mosaic phase and the origin of Mott-insulating state in 1T-TaS_2 *Nat. Commun.* **7** 10956

[29] Perfetti L, Georges A, Florens S, Biermann S, Mitrovic S, Berger H, Tomm Y, Höchst H and Grioni M 2003 Spectroscopic signatures of a bandwidth-controlled Mott transition at the surface of 1T-$TaSe_2$ *Phys. Rev. Lett.* **90** 166401

[30] Shi Y *et al* 2013 A ferroelectric-like structural transition in a metal *Nat. Mater.* **12** 1024

[31] Shi Y G *et al* 2009 Continuous metal-insulator transition of the antiferromagnetic perovskite $NaOsO_3$ *Phys. Rev.* B **80** 161104

[32] Jung M-C, Song Y-J, Lee K-W and Pickett W E 2013 Structural and correlation effects in the itinerant insulating antiferromagnetic perovskite $NaOsO_3$ *Phys. Rev.* B **87** 115119

[33] Calder S *et al* 2012 Magnetically driven metal-insulator transition in $NaOsO_3$ *Phys. Rev. Lett.* **108** 257209

[34] Du Y, Wan X, Sheng L, Dong J and Savrasov S Y 2012 Electronic structure and magnetic properties of $NaOsO_3$ *Phys. Rev.* B **85** 174424

[35] Lo Vecchio I, Perucchi A, Di Pietro P, Limaj O, Schade U, Sun Y, Arai M, Yamaura K and Lupi S 2013 Infrared evidence of a Slater metal-insulator transition in $NaOsO_3$ *Sci. Rep.* **3** 2990

[36] Calder S *et al* 2015 Enhanced spin-phonon-electronic coupling in a 5*d* oxide *Nat. Commun.* **6** 8916

[37] Khaliullin G 2013 Excitonic magnetism in Van Vleck-type d^4 Mott insulators *Phys. Rev. Lett.* **111** 197201

[38] Subedi A 2012 First-principles study of the electronic structure and magnetism of $CaIrO_3$ *Phys. Rev.* B **85** 020408

[39] Moretti Sala M, Ohgushi K, Al-Zein A, Hirata Y, Monaco G and Krisch M 2014 $CaIrO_3$: a spin–orbit Mott insulator beyond the $J_{\rm eff} = 1/2$ ground state *Phys. Rev. Lett.* **112** 176402

[40] Kim S-W, Liu C, Kim H-J, Lee J-H, Yao Y, Ho K-M and Cho J-H 2015 Nature of the insulating ground state of the 5*d* postperovskite $CaIrO_3$ *Phys. Rev. Lett.* **115** 096401

[41] Bremholm M, Dutton S E, Stephens P W and Cava R J 2011 $NaIrO_3$–a pentavalent post-perovskite *J. Solid State Chem.* **184** 601–7

[42] Du L, Sheng X, Weng H and Dai X 2013 The electronic structure of $NaIrO_3$, Mott insulator or band insulator? *Europhys. Lett.* **101** 27003

[43] Maiti K, Singh Ra S, Medicherla V R R, Rayaprol S and Sampathkumaran E V 2005 Origin of charge density wave formation in insulators from a high resolution photoemission study of $BaIrO_3$ *Phys. Rev. Lett.* **95** 016404

[44] Cheng J-G, Zhou J-S, Alonso J A, Goodenough J B, Sui Y, Matsubayashi K and Uwatoko Y 2009 Transition from a weak ferromagnetic insulator to an exchange-enhanced paramagnetic metal in the $BaIrO_3$ polytypes *Phys. Rev.* B **80** 104430

[45] Ju W, Liu G-Q and Yang Z 2013 Exotic spin-orbital Mott insulating states in $BaIrO_3$ *Phys. Rev.* B **87** 075112

[46] Moon S J *et al* 2008 Dimensionality-controlled insulator-metal transition and correlated metallic state in 5*d* transition metal oxides $Sr_{n+1}Ir_nO_{3n+1}$ ($n = 1$, 2, and ∞) *Phys. Rev. Lett.* **101** 226402

[47] Cao G, Durairaj V, Chikara S, DeLong L E, Parkin S and Schlottmann P 2007 Non-Fermi-liquid behavior in nearly ferromagnetic $SrIrO_3$ single crystals *Phys. Rev.* B **76** 100402

[48] Nie Y F *et al* 2015 Interplay of spin–orbit interactions, dimensionality and octahedral rotations in semimetallic $SrIrO_3$ *Phys. Rev. Lett.* **114** 016401

[49] Moon S J 2014 Temperature dependence of the optical response of perovskite-type $SrIrO_3$ thin film *J. Korean Phys. Soc.* **64** 1174–8

[50] Singh Y and Gegenwart P 2010 Antiferromagnetic Mott insulating state in single crystals of the honeycomb lattice material Na_2IrO_3 *Phys. Rev.* B **82** 064412

[51] Comin R *et al* 2012 Na_2IrO_3 as a novel relativistic Mott insulator with a 340 meV gap *Phys. Rev. Lett.* **109** 266406

[52] Liu X, Berlijn T, Yin W-G, Ku W, Tsvelik A, Kim Y-J, Gretarsson H, Singh Y, Gegenwart P and Hill J P 2011 Long-range magnetic ordering in Na_2IrO_3 *Phys. Rev.* B **83** 220403

[53] Gretarsson H *et al* 2013 Crystal-field splitting and correlation effect on the electronic structure of A_2IrO_3 *Phys. Rev. Lett.* **110** 076402

[54] Chaloupka J and Khaliullin G 2015 Hidden symmetries of the extended Kitaev-Heisenberg model: implications for the honeycomb-lattice iridates A_2IrO_3 *Phys. Rev.* B **92** 024413

[55] Chaloupka J and Khaliullin G 2016 Magnetic anisotropy in the Kitaev model systems Na_2IrO_3 and $RuCl_3$ *Phys. Rev.* B **94** 064435

[56] Singh Y, Manni S, Reuther J, Berlijn T, Thomale R, Ku W, Trebst S and Gegenwart P 2012 Relevance of the Heisenberg–Kitaev model for the honeycomb lattice iridates A_2IrO_3 *Phys. Rev. Lett.* **108** 127203

[57] Reuther J, Thomale R and Rachel S 2014 Spiral order in the honeycomb iridate Li_2Iro_3 *Phys. Rev.* B **90** 100405

[58] Biffin A, Johnson R D, Choi S, Freund F, Manni S, Bombardi A, Manuel P, Gegenwart P and Coldea R 2014 Unconventional magnetic order on the hyperhoneycomb Kitaev lattice in β-Li_2IrO_3: full solution via magnetic resonant x-ray diffraction *Phys. Rev.* B **90** 205116

[59] Takayama T, Kato A, Dinnebier R, Nuss J, Kono H, Veiga L S I, Fabbris G, Haskel D and Takagi H 2015 Hyperhoneycomb iridate β-Li_2IrO_3 as a platform for Kitaev magnetism *Phys. Rev. Lett.* **114** 077202

[60] Biffin A, Johnson R D, Kimchi I, Morris R, Bombardi A, Analytis J G, Vishwanath A and Coldea R 2014 Noncoplanar and counterrotating incommensurate magnetic order stabilized by Kitaev interactions in γ-Li_2IrO_3 *Phys. Rev. Lett.* **113** 197201

[61] Okabe H, Takeshita N, Isobe M, Takayama-Muromachi E, Muranaka T and Akimitsu J 2011 Pressure-induced metal-insulator transition in the spin–orbit Mott insulator Ba_2IrO_4 *Phys. Rev.* B **84** 115127

[62] Arita R, Kuneš J, Kozhevnikov A V, Eguiluz A G and Imada M 2012 *Ab initio* studies on the interplay between spin–orbit interaction and Coulomb correlation in Sr_2IrO_4 and Ba_2IrO_4 *Phys. Rev. Lett.* **108** 086403

[63] Katukuri V M, Stoll H, van den Brink J and Hozoi L 2012 *Ab initio* determination of excitation energies and magnetic couplings in correlated quasi-two-dimensional iridates *Phys. Rev.* B **85** 220402

[64] Moser S *et al* 2014 The electronic structure of the high-symmetry perovskite iridate Ba_2IrO_4 *New J. Phys.* **16** 013008

[65] Calder S, Cao G-X, Okamoto S, Kim J W, Cooper V R, Gai Z, Sales B C, Lumsden M D, Mandrus D and Christianson A D 2014 $J_{\rm eff} = \frac{1}{2}$ Mott spin–orbit insulating state close to the cubic limit in Ca_4Ir0_6 *Phys. Rev.* B **89** 081104

[66] Cao G, Durairaj V, Chikara S, Parkin S and Schlottmann P 2007 Partial antiferromagnetism in spin-chain $Sr_5Rh_4O_{12}$, $Ca_5Ir_3O_{12}$ and Ca_4IrO_6 single crystals *Phys. Rev.* B **75** 134402

[67] Franke I, Baker P J, Blundell S J, Lancaster T, Hayes W, Pratt F L and Cao G 2011 Measurement of the internal magnetic field in the correlated iridates Ca_4Iro_6, $Ca_5Ir_3O_{12}$, $Sr_3Ir_2O_7$ and Sr_2IrO_4 *Phys. Rev.* B **83** 094416

[68] Shapiro M C, Riggs S C, Stone M B, de la Cruz C R, Chi S, Podlesnyak A A and Fisher I R 2012 Structure and magnetic properties of the pyrochlore iridate $Y_2Ir_2O_7$ *Phys. Rev.* B **85** 214434

[69] Disseler S M 2014 Direct evidence for the all-in/all-out magnetic structure in the pyrochlore iridates from muon spin relaxation *Phys. Rev.* B **89** 140413

[70] Matsuhira K, Wakeshima M, Hinatsu Y and Takagi S 2011 Metal–insulator transitions in pyrochlore oxides $Ln_2Ir_2O_7$ *J. Phys. Soc. Japan* **80** 094701

[71] Kondo T *et al* 2015 Quadratic Fermi node in a 3D strongly correlated semimetal *Nat. Commun.* **6** 10042

[72] Matsuhira K, Wakeshima M, Nakanishi R, Yamada T, Nakamura A, Kawano W, Takagi S and Hinatsu Y 2007 Metal-insulator transition in pyrochlore iridates $Ln_2Ir_2O_7$ (Ln = Nd, Sm and Eu) *J. Phys. Soc. Japan* **76** 043706

[73] Sagayama H, Uematsu D, Arima T, Sugimoto K, Ishikawa J J, O'Farrell E and Nakatsuji S 2013 Determination of long-range all-in/all-out ordering of Ir^{4+} moments in a pyrochlore iridate $Eu_2Ir_2O_7$ by resonant x-ray diffraction *Phys. Rev.* B **87** 100403

[74] Sushkov A B, Hofmann J B, Jenkins G S, Ishikawa J, Nakatsuji S, Das Sarma S and Drew H D 2015 Optical evidence for a weyl semimetal state in pyrochlore $Eu_2Ir_2O_7$ *Phys. Rev.* B **92** 241108

[75] Uematsu D, Sagayama H, Arima T, Ishikawa J J, Nakatsuji S, Takagi H, Yoshida M, Mizuki J and Ishii K 2015 Large trigonal-field effect on spin–orbit coupled states in a pyrochlore iridate *Phys. Rev.* B **92** 094405

[76] Lefrançois E, Simonet V, Ballou R, Lhotel E, Hadj-Azzem A, Kodjikian S, Lejay P, Manuel P, Khalyavin D and Chapon L C 2015 Anisotropy-tuned magnetic order in pyrochlore iridates *Phys. Rev. Lett.* **114** 247202

[77] Disseler S M, Dhital C, Amato A, Giblin S R, de la Cruz C, Wilson S D and Graf M J 2012 Magnetic order in the pyrochlore iridates $A_2Ir_2O_7$ (A = Y, Yb) *Phys. Rev.* B **86** 014428

[78] Taira N, Wakeshima M and Hinatsu Y 2001 Magnetic properties of iridium pyrochlores $R_2Ir_2O_7$ (R = Y, Sm, Eu and Lu) *J. Phys.: Condens. Matter* **13** 5527

[79] Lee Y S, Moon S J, Riggs S C, Shapiro M C, Fisher I R, Fulfer B W, Chan J Y, Kemper A F and Basov D N 2013 Infrared study of the electronic structure of the metallic pyrochlore iridate $Bi_2Ir_2O_7$ *Phys. Rev.* B **87** 195143

[80] Qi T F, Korneta O B, Wan X, DeLong L E, Schlottmann P and Cao G 2012 Strong magnetic instability in correlated metallic $Bi_2Ir_2O_7$ *J. Phys.: Condens. Matter* **24** 345601

[81] Cao G, Xin Y, Alexander C S, Crow J E, Schlottmann P, Crawford M K, Harlow R L and Marshall W 2002 Anomalous magnetic and transport behavior in the magnetic insulator $Sr_3Ir_2O_7$ *Phys. Rev.* B **66** 214412

[82] Fujiyama S, Ohashi K, Ohsumi H, Sugimoto K, Takayama T, Komesu T, Takata M, Arima T and Takagi H 2012 Weak antiferromagnetism of $J_{\rm eff} = \frac{1}{2}$ band in bilayer iridate $Sr_3Ir_2O_7$ *Phys. Rev.* B **86** 174414

[83] Park H J, Sohn C H, Jeong D W, Cao G, Kim K W, Moon S J, Jin H, Cho D-Y and Noh T W 2014 Phonon-assisted optical excitation in the narrow bandgap Mott insulator $Sr_3Ir_2O_7$ *Phys. Rev.* B **89** 155115

[84] Hogan T, Bjaalie L, Zhao L, Belvin C, Wang X, Van de Walle C G, Hsieh D and Wilson S D 2016 Structural investigation of the bilayer iridate $Sr_3Ir_2O_7$ *Phys. Rev.* B **93** 134110

[85] Kim J, Said A H, Casa D, Upton M H, Gog T, Daghofer M, Jackeli G, van den Brink J, Khaliullin G and Kim B J 2012 Large spin-wave energy gap in the bilayer iridate $Sr_3Ir_2O_7$: evidence for enhanced dipolar interactions near the Mott metal-insulator transition *Phys. Rev. Lett.* **109** 157402

[86] Okamoto Y, Nohara M, Aruga-Katori H and Takagi H 2007 Spin-liquid state in the $S = 1/2$ hyperkagome antiferromagnet $Na_4Ir_3O_8$ *Phys. Rev. Lett.* **99** 137207

[87] Dally R, Hogan T, Amato A, Luetkens H, Baines C, Rodriguez-Rivera J, Graf M J and Wilson S D 2014 Short-range correlations in the magnetic ground state of $Na_4Ir_3O_8$ *Phys. Rev. Lett.* **113** 247601

[88] Balodhi A, Thamizhavel A and Singh Y 2015 Evolution of magnetic, transport and thermal properties in $Na_{4-x}Ir_3O_8$ *Phys. Rev.* B **91** 224409

[89] Wakeshima M, Taira N, Hinatsu Y and Ishii Y 2003 Electrical and magnetic properties of pseudo-one-dimensional calcium iridium oxide $Ca_5Ir_3O_{12}$ *Solid State Commun.* **125** 311–5

[90] Cao G, Subedi A, Calder S, Yan J-Q, Yi J, Gai Z, Poudel L, Singh D J, Lumsden M D, Christianson A D, Sales B C and Mandrus D 2013 Magnetism and electronic structure of La_2ZnIrO_6 and La_2MgIrO_6: candidate $J_{\rm eff} = \frac{1}{2}$ Mott insulators *Phys. Rev.* B **87** 155136

[91] Ghimire M P, Wu L-H and Hu X 2016 Possible half-metallic antiferromagnetism in an iridium double-perovskite material *Phys. Rev.* B **93** 134421

[92] Mugavero S J III, Fox A H, Smith M D and zur Loye H-C 2010 Crystal growth, structure and magnetic properties of the double perovskites Ln_2MgIrO_6 (Ln = Pr, Nd, Sm–Gd) *J. Solid State Chem.* **183** 465–70

[93] Harada D, Wakeshima M and Hinatsu Y 1999 The structure and magnetic properties of new iridium (IV) perovskites Sr_2LnIrO_6 (Ln = Ce, Tb) *J. Solid State Chem.* **145** 356–60

[94] Panda S K and Dasgupta I 2013 Electronic structure and magnetism in Ir-based double-perovskite Sr_2CeIrO_6 *Mod. Phys. Lett.* B **27** 1350041

[95] Kanungo S, Mogare K, Yan B, Felser C and Jansen M 2016 Orbital ordering of Ir-t_{2g} states in the double perovskite Sr_2CeIrO_6 *Phys. Rev.* B **93** 245148

[96] Dey T *et al* 2016 Ba_2YIrO_6: a cubic double perovskite material with Ir^{5+} ions *Phys. Rev.* B **93** 014434

[97] Dey T, Mahajan A V, Khuntia P, Baenitz M, Koteswararao B and Chou F C 2012 Spin-liquid behavior in $J_{\rm eff} = \frac{1}{2}$ triangular lattice compound $Ba_3IrTi_2O_9$ *Phys. Rev.* B **86** 140405

[98] Catuneanu A, Rau J G, Kim H-S and Kee H-Y 2015 Magnetic orders proximal to the Kitaev limit in frustrated triangular systems: application to $Ba_3IrTi_2O_9$ *Phys. Rev.* B **92** 165108

[99] Dey T, Kumar R, Mahajan A V, Kaushik S D and Siruguri V 2014 Unconventional magnetism in the spin–orbit-driven Mott insulators $Ba_3MIr_2O_9$ ($M = Sc, Y$) *Phys. Rev.* B **89** 205101

[100] Nag A *et al* 2016 Origin of the spin–orbital liquid state in a nearly $j = 0$ iridate $Ba_3ZnIr_2O_9$ *Phys. Rev. Lett.* **116** 097205

[101] Zhou J-S, Matsubayashi K, Uwatoko Y, Jin C-Q, Cheng J-G, Goodenough J B, Liu Q Q, Katsura T, Shatskiy A and Ito E 2008 Critical behavior of the ferromagnetic perovskite $BaRuO_3$ *Phys. Rev. Lett.* **101** 077206

[102] Jin C-Q *et al* 2008 High-pressure synthesis of the cubic perovskite $BaRuO_3$ and evolution of ferromagnetism in $ARuO_3$ (A = Ca, Sr, Ba) ruthenates *Proc. Natl Acad. Sci.* 105 7115–9

[103] Han Q, Dang H T and Millis A J 2016 Ferromagnetism and correlation strength in cubic barium ruthenate in comparison to strontium and calcium ruthenate: a dynamical mean-field study *Phys. Rev.* B **93** 155103

[104] Longo J M, Raccah P M and Goodenough J B 1968 Magnetic properties of $SrRuO_3$ and $CaRuO_3$ *J. Appl. Phys.* **39** 1327–8

[105] Schneider M *et al* 2014 Low-energy electronic properties of clean $CaRuO_3$: elusive Landau quasiparticles *Phys. Rev. Lett.* **112** 206403

[106] Capogna L *et al* 2002 Sensitivity to disorder of the metallic state in the ruthenates *Phys. Rev. Lett.* **88** 076602

[107] Noro Y and Miyahara S 1969 Electrical resistivity of $SrRuO_3$ *J. Phys. Soc. Japan* **27** 518A

[108] Fatuzzo C G *et al* 2015 Spin–orbit-induced orbital excitations in Sr_2RuO_4 and Ca_2RuO_4: a resonant inelastic x-ray scattering study *Phys. Rev.* B **91** 155104

[109] Zhang G, Gorelov E, Sarvestani E and Pavarini E 2016 Fermi surface of Sr_2RuO_4: spin–orbit and anisotropic Coulomb interaction effects *Phys. Rev. Lett.* **116** 106402

[110] Alexander C S, Cao G, Dobrosavljevic V, McCall S, Crow J E, Lochner E and Guertin R P 1999 Destruction of the Mott insulating ground state of Ca_2RuO_4 by a structural transition *Phys. Rev.* B **60** R8422–5

[111] Mizokawa T, Tjeng L H, Sawatzky G A, Ghiringhelli G, Tjernberg O, Brookes N B, Fukazawa H, Nakatsuji S and Maeno Y 2001 Spin–orbit coupling in the Mott insulator Ca_2RuO_4 *Phys. Rev. Lett.* **87** 077202

[112] Liu G-Q 2013 Competition between spin–orbit coupling and magnetic exchange splitting in Ca_2RuO_4 *Phys. Rev.* B **88** 104428

[113] Tian W *et al* 2015 High antiferromagnetic transition temperature of the honeycomb compound $SrRu_2O_6$ *Phys. Rev.* B **92** 100404

[114] Hiley C I *et al* 2015 Antiferromagnetism at $T > 500\ K$ in the layered hexagonal ruthenate $SrRu_2O_6$ *Phys. Rev.* B **92** 104413

[115] Tamai A *et al* 2008 Fermi surface and van Hove singularities in the itinerant metamagnet $Sr_3Ru_2O_7$ *Phys. Rev. Lett.* **101** 026407

[116] Mao Z Q, Zhou M, Hooper J, Golub V and O'Connor C J 2006 Phase separation in the itinerant metamagnetic transition of $Sr_4Ru_3O_{10}$ *Phys. Rev. Lett.* **96** 077205

[117] Granata V, Capogna L, Forte F, Lepetit M-B, Fittipaldi R, Stunault A, Cuoco M and Vecchione A 2016 Spin-orbital nature of the high-field magnetic state in the $Sr_4Ru_3O_{10}$ *Phys. Rev.* B **93** 115128

[118] Luo Y, Cao C, Si B, Li Y, Bao J, Guo H, Yang X, Shen C, Feng C, Dai J, Cao G and Xu Z 2013 Li_2Rho_3: a spin-glassy relativistic Mott insulator *Phys. Rev.* B **87** 161121

[119] Mazin I I, Manni S, Foyevtsova K, Jeschke H O, Gegenwart P and Valentí R 2013 Origin of the insulating state in honeycomb iridates and rhodates *Phys. Rev.* B **88** 035115

[120] Baumberger F, Ingle N J C, Meevasana W, Shen K M, Lu D H, Perry R S, Mackenzie A P, Hussain Z, Singh D J and Shen Z-X 2006 Fermi surface and quasiparticle excitations of Sr_2RhO_4 *Phys. Rev. Lett.* **96** 246402

[121] Perry R S, Baumberger F, Balicas L, Kikugawa N, Ingle N J C, Rost A, Mercure J F, Maeno Y, Shen Z X and Mackenzie A P 2006 Sr_2RhO_4: a new, clean correlated electron metal *New J. Phys.* **8** 175

[122] Calder S, Li L, Okamoto S, Choi Y, Mukherjee R, Haskel D and Mandrus D 2015 Spin–orbit driven magnetic insulating state with $J_{\text{eff}} = \frac{1}{2}$ character in a 4*d* oxide *Phys. Rev.* B **92** 180413

[123] Cao G, Parkin S and Schlottmann P 2007 Magnetic anisotropy and geometrical frustration in the Ising spin-chain system $Sr_5Rh_4O_{12}$ *Solid State Commun.* **141** 369– 373

[124] Jung M-C and Lee K-W 2014 Electronic structures, magnetism and phonon spectra in the metallic cubic perovskite $BaOsO_3$ *Phys. Rev.* B **90** 045120

[125] Shi Y *et al* 2013 High-pressure synthesis of 5*d* cubic perovskite $BaOsO_3$ at 17 GPa: ferromagnetic evolution over 3d to 5d series *J. Am. Chem. Soc.* **135** 16507–16

[126] Mandrus D, Thompson J R, Gaal R, Forro L, Bryan J C, Chakoumakos B C, Woods L M, Sales B C, Fishman R S and Keppens V 2001 Continuous metal–insulator transition in the pyrochlore $Cd_2Os_2O_7$ *Phys. Rev.* B **63** 195104

[127] Padilla W J, Mandrus D and Basov D N 2002 Searching for the Slater transition in the pyrochlore $Cd_2Os_2O_7$ with infrared spectroscopy *Phys. Rev.* B **66** 035120

[128] Bogdanov N A, Maurice R, Rousochatzakis I, van den Brink J. and Hozoi L 2013 Magnetic state of pyrochlore $Cd_2Os_2O_7$ emerging from strong competition of ligand distortions and longer-range crystalline anisotropy *Phys. Rev. Lett.* **110** 127206

[129] Sohn C H *et al* 2015 Optical spectroscopic studies of the metal–insulator transition driven by all-in/all-out magnetic ordering in 5*d* pyrochlore $Cd_2Os_2O_7$ *Phys. Rev. Lett.* **115** 266402

[130] Lee K-W and Pickett W E 2007 Orbital-quenching-induced magnetism in Ba_2NaOsO_6 *Europhys. Lett.* **80** 37008

[131] Steele A J, Baker P J, Lancaster T, Pratt F L, Franke I, Ghannadzadeh S, Goddard P A, Hayes W, Prabhakaran D and Blundell S J 2011 Low-moment magnetism in the double perovskites Ba_2MOsO_6 (M = Li,Na) *Phys. Rev.* B **84** 144416

[132] Gangopadhyay S and Pickett W E 2015 Spin–orbit coupling, strong correlation and insulator-metal transitions: the $j_{\text{eff}} = \frac{3}{2}$ ferromagnetic Dirac–Mott insulator Ba_2NaOsO_6 *Phys. Rev.* B **91** 045133

[133] Thompson C M *et al* 2014 Long-range magnetic order in the $5d^2$ double perovskite Ba_2CaOsO_6 : comparison with spin-disordered Ba_2YReO_6 *J. Phys.: Condens. Matter* **26** 306003

[134] Gangopadhyay S and Pickett W E 2016 Interplay between spin–orbit coupling and strong correlation effects: comparison of the three osmate double perovskites Ba_2AOsO_6 (A = Na, Ca, Y) *Phys. Rev.* B **93** 155126

[135] Kermarrec E *et al* 2015 Frustrated fcc antiferromagnet Ba_2YOsO_6: structural characterization, magnetic properties and neutron scattering studies *Phys. Rev.* B **91** 075133

[136] Huang Q, Soubeyroux J L, Chmaissem O, Natali Sora I, Santoro A, Cava R J, Krajewski J J and Peck W F 1994 Neutron powder diffraction study of the crystal structures of Sr_2RuO_4 and Sr_2IrO_4 at room temperature and at 10 K *J. Solid State Chem.* **112** 355

[137] Moon S J, Jin H, Choi W S, Lee J S, Seo S S A, Yu J, Cao G, Noh T W and Lee Y S 2009 Temperature dependence of the electronic structure of the $J_{\text{eff}} = \frac{1}{2}$ Mott insulator Sr_2IrO_4 studied by optical spectroscopy *Phys. Rev.* B **80** 195110

[138] Cao G, Bolivar J, McCall S, Crow J E and Guertin R P 1998 Weak ferromagnetism, metal-to-nonmetal transition and negative differential resistivity in single-crystal Sr_2IrO_4 *Phys. Rev.* B **57** R11039

[139] Jin H, Jeong H, Ozaki T and Yu J 2009 Anisotropic exchange interactions of spin–orbit-integrated states in Sr_2IrO_4 *Phys. Rev.* B **80** 075112

[140] Watanabe H, Shirakawa T and Yunoki S 2010 Microscopic Study of a spin–orbit-Induced Mott Insulator in Ir oxides *Phys. Rev. Lett.* **105** 216410

[141] Fujiyama S, Ohsumi H, Ohashi K, Hirai D, Kim B J, Arima T, Takata M and Takagi H 2014 Spin and orbital contributions to magnetically ordered moments in 5*d* layered perovskite Sr_2IrO_4 *Phys. Rev. Lett.* **112** 016405

[142] Liu P, Khmelevskyi S, Kim B, Marsman M, Li D, Chen X-Q, Sarma D D, Kresse G and Franchini C 2015 Anisotropic magnetic couplings and structure-driven canted to collinear transitions in Sr_2IrO_4 by magnetically constrained noncollinear DFT *Phys. Rev.* B **92** 054428

[143] Dai J, Calleja E, Cao G and McElroy K 2014 Local density of states study of a spin–orbit-coupling induced Mott insulator Sr_2IrO_4 *Phys. Rev.* B **90** 041102

[144] Brouet V *et al* 2015 Transfer of spectral weight across the gap of Sr_2IrO_4 induced by La doping *Phys. Rev.* B **92** 081117

[145] Piovera C, Brouet V, Papalazarou E, Caputo M, Marsi M, Taleb-Ibrahimi A, Kim B J and Perfetti L 2016

Time-resolved photoemission of Sr_2IrO_4 *Phys. Rev.* B **93** 241114

[146] Hsieh D, Mahmood F, Torchinsky D H, Cao G and Gedik N 2012 Observation of a metal-to-insulator transition with both Mott-Hubbard and Slater characteristics in Sr_2IrO_4 from time-resolved photocarrier dynamics *Phys. Rev.* B **86** 035128

[147] Birol T and Haule K 2015 $J_{\rm eff} = 1/2$ Mott-insulating state in Rh and Ir fluorides *Phys. Rev. Lett.* **114** 096403

[148] de la Torre A *et al* 2015 Collapse of the Mott gap and emergence of a nodal liquid in lightly doped Sr_2IrO_4 *Phys. Rev. Lett.* **115** 176402

[149] Hogan T *et al* 2015 First-order melting of a weak spin–orbit Mott insulator into a correlated metal *Phys. Rev. Lett.* **114** 257203

[150] Cheng J-G, Zhou J-S, Goodenough J B, Sui Y, Ren Y and Suchomel M R 2011 High-pressure synthesis and physical properties of perovskite and post-perovskite $Ca_{1-x}Sr_xIrO_3$ *Phys. Rev.* B **83** 064401

[151] Gunasekera J, Harriger L, Dahal A, Heitmann T, Vignale G and Singh D K 2015 Magnetic fluctuations driven insulator-to-metal transition in $CaIr_{1-x}Ru_xO_3$ *Sci. Rep.* **5** 18047

[152] Qi T F, Korneta O B, Li L, Butrouna K, Cao V S, Wan X, Schlottmann P, Kaul R K and Cao G 2012 Spin–orbit tuned metal-insulator transitions in single-crystal $Sr_2Ir_{1-x}Rh_xO_4$ ($0 \leqslant x \leqslant 1$) *Phys. Rev.* B **86** 125105

[153] Chikara S êt al 2015 $Sr_2Ir_{1-x}Rh_xO_4$ ($x < 0.5$): an inhomogeneous $J_{\rm eff} = \frac{1}{2}$ Hubbard system *Phys. Rev.* B **92** 081114

[154] Calder S *et al* 2015 Evolution of competing magnetic order in the $J_{\rm eff} = 1/2$ insulating state of $Sr_2Ir_{1-x}Ru_xO_4$ *Phys. Rev.* B **92** 165128

[155] Phelan B F, Krizan J, Xie W, Gibson Q and Cava R J 2015 New material for probing spin–orbit coupling in iridates *Phys. Rev.* B **91** 155117

[156] Liu G-Q 2011 Spin–orbit coupling induced Mott transition in $Ca_{2-x}Sr_xRuO_4$ ($0 \leqslant x \leqslant 0.2$) *Phys. Rev.* B **84** 235136

[157] Kim W J, Kim S Y, Kim C H, Sohn C H, Korneta O B, Chae S C and Noh T W 2016 Spin–orbit coupling induced band structure change and orbital character of epitaxial IrO_2 films *Phys. Rev.* B **93** 045104

[158] Panda S K, Bhowal S, Delin A, Eriksson O and Dasgupta I 2014 Effect of spin orbit coupling and Hubbard U on the electronic structure of IrO_2 *Phys. Rev.* B **89** 155102

[159] Kahk J M *et al* 2014 Understanding the electronic structure of IrO_2 using hard-x-ray photoelectron spectroscopy and density-functional theory *Phys. Rev. Lett.* **112** 117601

[160] Figgis B N and Lewis J 2007 *The Magnetic Properties of Transition Metal Complexes* (New York: Wiley) pp 37–239

[161] Schwerdtfeger P 2004 *Relativistic Electronic Structure Theory, Part 2: Applications* (Amsterdam: Elsevier)

[162] Friedel J 1969 *The Physics of Metals, Electrons* ed J M Ziman (Cambridge: Cambridge University Press)

[163] Calder S, Cao G-X, Lumsden M D, Kim J W, Gai Z, Sales B C, Mandrus D and Christianson A D 2012 Magnetic structural change of Sr_2IrO_4 upon Mn doping *Phys. Rev.* B **86** 220403

[164] Lichtenstein A I and Katsnelson M I 1998 *Ab initio* calculations of quasiparticle band structure in correlated systems: LDA + + approach *Phys. Rev.* B **57** 6884

[165] Anisimov V I, Poteryaev A I, Korotin M A, Anokhin A O and Kotliar G 1997 First-principles calculations of the electronic structure and spectra of strongly correlated systems: dynamical mean-field theory *J. Phys.: Condens. Matter* **9** 7359

[166] Biermann S 2006 Electronic structure of transition metal compounds: DFT-DMFT approach in *Encyclopedia of Materials: Science and Technology* 2nd edn (Oxford: Elsevier) pp 1–9

[167] Biermann S 2014 Dynamical screening effects in correlated electron materials—a progress report on combined many-body perturbation and dynamical mean field theory: GW+DMFT *J. Phys.: Condens. Matter* **26** 173202

[168] Biermann S, Dallmeyer A, Carbone C, Eberhardt W, Pampuch C, Rader O, Katsnelson M I and Lichtenstein A I 2004 Observation of Hubbard bands in γ-manganese *JETP Lett.* **80** 612

[169] Lichtenstein A I, Katsnelson M I and Kotliar G 2001 Finite-temperature magnetism of transition metals: an *ab initio* dynamical mean-field theory *Phys. Rev. Lett.* **87** 067205

[170] Braun J, Minár J, Ebert H, Katsnelson M I and Lichtenstein A I 2006 Spectral function of ferromagnetic 3*d* metals: a self-consistent LSDA+DMFT approach combined with the one-step model of photoemission *Phys. Rev. Lett.* **97** 227601

[171] Sánchez-Barriga J *et al* 2010 Quantitative determination of spin-dependent quasiparticle lifetimes and electronic correlations in hcp cobalt *Phys. Rev.* B **82** 104414

[172] Biermann S, Poteryaev A, Lichtenstein A I and Georges A 2005 Dynamical singlets and correlation-assisted Peierls transition in VO_2 *Phys. Rev. Lett.* **94** 026404

[173] Tomczak J M and Biermann S 2007 Effective band structure of correlated materials: the case of VO_2 *J. Phys.: Condens. Matter* **19** 365206

[174] Tomczak J M and Biermann S 2009 Materials design using correlated oxides: optical properties of vanadium dioxide *Europhys. Lett.* **86** 37004

[175] Tomczak J M and Biermann S 2009 Optical properties of correlated materials: generalized Peierls approach and its application to VO_2 *Phys. Rev.* B **80** 085117

[176] Tomczak J M and Biermann S 2009 Multi-orbital effects in optical properties of vanadium sesquioxide *J. Phys.: Condens. Matter* **21** 064209

[177] Thunström P, Di Marco I and Eriksson O 2012 Electronic entanglement in late transition metal oxides *Phys. Rev. Lett.* **109** 186401

[178] Lechermann F, Biermann S and Georges A 2007 Competing itinerant and localized states in strongly correlated $BaVS_3$ *Phys. Rev.* B **76** 085101

[179] Lechermann F, Biermann S and Georges A 2005 Importance of interorbital charge transfers for the metal-to-insulator transition of $BaVS_3$ *Phys. Rev. Lett.* **94** 166402

[180] Aichhorn M, Pourovskii L, Vildosola V, Ferrero M, Parcollet O, Miyake T, Georges A and Biermann S 2009 Dynamical mean-field theory within an augmented plane-wave framework: assessing electronic correlations in the iron pnictide LaFeAsO *Phys. Rev.* B **80** 085101

[181] Miyake T, Nakamura K, Arita R and Imada M 2010 Comparison of *ab initio* low-energy models for LaFePO, LaFeAsO, $BaFe_2As_2$, LiFeAs, FeSe and FeTe: electron correlation and covalency *J. Phys. Soc. Japan* **79** 044705

[182] Amadon B, Biermann S, Georges A and Aryasetiawan F 2006 The α-γ transition of cerium is entropy driven *Phys. Rev. Lett.* **96** 066402

[183] Zölfl M B, Nekrasov I A, Pruschke T, Anisimov V I and Keller J 2001 Spectral and magnetic properties of α- and γ-Ce from dynamical mean-field theory and local density approximation *Phys. Rev. Lett.* **87** A266403

[184] Bieder J and Amadon B 2014 Thermodynamics of the α-γ transition in cerium from first principles *Phys. Rev.* B **89** 195132

[185] Pourovskii L V, Amadon B, Biermann S and Georges A 2007 Self-consistency over the charge density in dynamical mean-field theory: a linear muffin-tin implementation and some physical implications *Phys. Rev.* B **76** 235101

[186] Miyake T, Pourovskii L, Vildosola V, Biermann S and Georges A 2008 d- and f-orbital correlations in the REFeAsO compounds *J. Phys. Soc. Japan* **77** 99–102

[187] Tomczak J M, Pourovskii L V, Vaugier L, Georges A and Biermann S 2013 Rare-earth versus heavy metal pigments and their colors from first principles *Proc. Natl Acad. Sci.* 110 904–7

[188] Haule K, Yee C-H and Kim K 2010 Dynamical mean-field theory within the full-potential methods: electronic structure of $CeIrIn_5$, $CeCoIn_5$ and $CeRhIn_5$ *Phys. Rev.* B **81** 195107

[189] Pourovskii L V, Hansmann P, Ferrero M and Georges A 2014 Theoretical prediction and spectroscopic fingerprints of an orbital transition in $CeCu_2Si_2$ *Phys. Rev. Lett.* **112** 106407

[190] Savrasov S Y, Kotliar G and Abrahams E 2001 Correlated electrons in δ-plutonium within a dynamical mean-field picture *Nature* **410** 793

[191] Savrasov S Y, Haule K and Kotliar G 2006 Many-body electronic structure of americium metal *Phys. Rev. Lett.* **96** 036404

[192] Kolorenc J, Shick A B and Lichtenstein A I 2015 Electronic structure and core-level spectra of light actinide dioxides in the dynamical mean-field theory *Phys. Rev.* B **92** 085125

[193] Pourovskii L V, Katsnelson M I and Lichtenstein A I 2005 Correlation effects in electronic structure of actinide monochalcogenides *Phys. Rev.* B **72** 115106

[194] Ferber J, Foyevtsova K, Jeschke H O and Valentí R 2014 Unveiling the microscopic nature of correlated organic conductors: the case of κ-$ET_2Cu[N(CN)_2]Br_xCl_{1-x}$ *Phys. Rev.* B **89** 205106

[195] Tomczak J M, Haule K, Miyake T, Georges A and Kotliar G 2010 Thermopower of correlated semiconductors: application to $FeAs_2$ and $FeSb_2$ *Phys. Rev.* B **82** 085104

[196] Sun P, Xu W, Tomczak J M, Kotliar G, Sondergaard M, Iversen B B and Steglich F 2013 Highly dispersive electron relaxation and colossal thermoelectricity in the correlated semiconductor $FeSb_2$ *Phys. Rev.* B **88** 245203

[197] Hirayama M, Miyake T and Imada M 2012 *Ab initio* low-energy model of transition-metal-oxide heterostructure $LaAlO_3/SrTiO_3$ *J. Phys. Soc. Japan* **81** 084708

[198] Hansmann P, Ayral T, Vaugier L, Werner P and Biermann S 2013 Long-range Coulomb interactions in surface systems: a first-principles description within self-consistently combined *GW* and dynamical mean-field theory *Phys. Rev. Lett.* **110** 166401

[199] Hansmann P, Ayral T, Tejeda A and Biermann S 2016 Uncertainty principle for experimental measurements: fast versus slow probes *Sci. Rep.* **6** 19728

[200] Biermann S, Aryasetiawan F and Georges A 2003 First-principles approach to the electronic structure of strongly correlated systems: combining the GW approximation and dynamical mean-field theory *Phys. Rev. Lett.* **90** 086402

[201] Ayral T, Werner P and Biermann S 2012 Spectral properties of correlated materials: local vertex and nonlocal two-particle correlations from combined GW and dynamical mean field theory *Phys. Rev. Lett.* **109** 226401

[202] Ayral T, Biermann S and Werner P 2013 Screening and nonlocal correlations in the extended Hubbard model from self-consistent combined GW and dynamical mean field theory *Phys. Rev.* B **87** 125149

[203] van Roekeghem A and Biermann S 2014 Screened exchange dynamical mean-field theory and its relation to density functional theory: $SrVO_3$ and $SrTiO_3$ *Europhys. Lett.* **108** 57003

[204] Vaugier L, Jiang H and Biermann S 2012 Hubbard *U* and Hund exchange *J* in transition metal oxides: screening versus localization trends from constrained random phase approximation *Phys. Rev.* B **86** 165105

[205] Anisimov V I *et al* 2005 Full orbital calculation scheme for materials with strongly correlated electrons *Phys. Rev.* B **71** 125119

[206] Lechermann F, Georges A, Poteryaev A, Biermann S, Posternak M, Yamasaki A and Andersen O K 2006 Dynamical mean-field theory using Wannier functions: a flexible route to electronic structure calculations of strongly correlated materials *Phys. Rev.* B **74** 125120

[207] Aichhorn M, Pourovskii L, Seth P, Vildosola V, Zingl M, Peil O E, Deng X, Mravlje J, Kraberger G J, Martins C, Ferrero M and Parcollet O 2016 TRIQS/DFTTools: a TRIQS application for *ab initio* calculations of correlated materials *Comput. Phys. Commun.* **204** 200–8

[208] Blaha P, Schwarz K, Madsen G, Kvasnicka D and Luitz J 2001 *Wien2k, An Augmented Plane Wave + Local Orbitals Program for Calculating Crystal Properties* ed K Schwarz (Austria: Tech. Universität Wien)

[209] Martins C 2010 Interplay of spin–orbit coupling and electronic Coulomb interactions in strontium iridate Sr_2IrO_4 *PhD Thesis* Ecole Polytechnique

[210] Shubnikov A V 1951 *Symmetry and Antisymmetry of Finite Figures* (Moscow: USSR Academy of Sciences)

[211] Aryasetiawan F, Imada M, Georges A, Kotliar G, Biermann S and Lichtenstein A I 2004 Frequency-dependent local interactions and low-energy effective models from electronic structure calculations *Phys. Rev.* B **70** 195104

[212] Miyake T and Aryasetiawan F 2008 Screened Coulomb interaction in the maximally localized Wannier basis *Phys. Rev.* B **77** 085122

[213] Aryasetiawan F, Karlsson K, Jepsen O and Schönberger U 2006 Calculations of Hubbard *U* from first-principles *Phys. Rev.* B **74** 125106

[214] Tomczak J M, Miyake T and Aryasetiawan F 2010 Realistic many-body models for manganese monoxide under pressure *Phys. Rev.* B **81** 115116

[215] Sakuma R and Aryasetiawan F 2013 First-principles calculations of dynamical screened interactions for the transition metal oxides *m*o (m = mn, fe, co, ni) *Phys. Rev.* B **87** 165118

[216] Nakamura K, Arita R and Imada M 2008 *Ab initio* derivation of low-energy model for iron-based superconductors LaFeAsO and LaFePO *J. Phys. Soc. Japan* **77** 093711

[217] Imada M and Miyake T 2010 Electronic structure calculation by first principles for strongly correlated electron systems *J. Phys. Soc. Japan* **79** 112001

[218] Nilsson F, Sakuma R and Aryasetiawan F 2013 *Ab initio* calculations of the Hubbard *U* for the early lanthanides using the constrained random-phase approximation *Phys. Rev.* B **88** 125123

[219] Hansmann P, Vaugier L, Jiang H and Biermann S 2013 What about U on surfaces? Extended Hubbard models for adatom systems frrom first principles *J. Phys.: Condens. Matter* **25** 094005

[220] Solovyev I V and Imada M 2005 Screening of coulomb interactions in transition metals *Phys. Rev.* B **71** 045103

[221] Şaşıoğlu E, Friedrich C and Blügel S 2011 Effective Coulomb interaction in transition metals from constrained random-phase approximation *Phys. Rev.* B **83** 121101

[222] Marzari N and Vanderbilt D 1997 Maximally localized generalized Wannier functions for composite energy bands *Phys. Rev.* B **56** 12847–65

[223] Werner P, Comanac A, de' Medici L, Troyer M and Millis A J 2006 Continuous-time solver for quantum impurity models *Phys. Rev. Lett.* **97** 076405

[224] Beach K S D 2004 Identifying the maximum entropy method as a special limit of stochastic analytic continuation (arXiv:cond-mat/0403055)

[225] Crawford M K, Subramanian M A, Harlow R L, Fernandez-Baca J A, Wang Z R and Johnston D C 1994 Structural and magnetic studies of Sr_2IrO_4 *Phys. Rev.* B **49** 9198
[226] Vogt T and Buttrey D J 1996 Temperature dependent structural behavior of Sr_2RhO_4 *J. Solid State Chem.* **123** 186–9
[227] Chmaissem O, Jorgensen J D, Shaked H, Ikeda S and Maeno Y 1998 Thermal expansion and compressibility of Sr_2RuO_4 *Phys. Rev.* B **57** 5067–70
[228] Florens S, Georges A, Kotliar G and Parcollet O 2002 Mott transition at large orbital degeneracy: dynamical mean-field theory *Phys. Rev.* B **66** 205102